Energy & Environmental Science

Chemical and structural evolution of Li-Mn-rich layered electrodes under different current densities

Journal:	*Energy & Environmental Science*
Manuscript ID	EE-ART-04-2022-001229.R1
Article Type:	Paper
Date Submitted by the Author:	14-Jul-2022
Complete List of Authors:	He, Xin; Sichuan University Wu, Jue; Xiamen University Zhu, Zhuoying; LBNL, ESDR Division Liu, Haodong; University of California San Diego, NanoEngineering Li, Ning; LBNL, ESDR Division Zhou, Dong; Ningbo Institute of Materials Technology & Engineering Zhou, Xu; Uppsala Universitet Zhang, Haowei; Sichuan University Bresser, Dominic; Karlsruhe Institute of Technology (KIT), Helmholtz Institute Ulm (HIU) Fu, Yanbo; Lawrence Berkeley National Laboratory, Crafton, Matthew; University of California Berkeley, Department of Chemical and Biomolecular Engineering; Lawrence Berkeley National Laboratory, Energy Storage and Distributed Resources Division McCloskey, Bryan; University of California Berkeley, Department of Chemical and Biomolecular Engineering; E O Lawrence Berkeley National Laboratory, Energy Storage and Distributed Resources Division Chen, Yan; ORNL, Chemical and Engineering Materials An, Ke; ORNL, Liu, Ping; University of California, San Diego, Department of Nanoengineering Jain, Anubhav; Lawrence Berkeley National Lab, Energy & Environmental Technologies Division Li, Jie; Department of Energy, Politecnico di Milano Yang, Wanli; Lawrence Berkeley National Laboratory, Advanced Light Source Yang, Yong; Xiamen University, State Key Lab for Physical Chemistry and Department of Chemistry Winter, Martin; Helmholtz Institute Muenster, IEK-12, Forschungszentrum Juelich Kostecki, Robert; LBNL, ESDR Division

Chemical and structural evolutions of Li-Mn-rich layered electrodes under different current densities

Xin He[a,b,c#*], Jue Wu[d,e#], Zhuoying Zhu[b#], Haodong Liu[f], Ning Li[b], Dong Zhou[g], Xu Hou[h], Jun Wang[g], Haowei Zhang[c], Dominic Bresser[i], Yanbao Fu[b], Matthew J Crafton[b,j], Bryan D McCloskey[b,j], Yan Chen[k], Ke An[k], Ping Liu[f], Anubhav Jain[b*], Jie Li[l*], Wanli Yang[d*], Yong Yang[e], Martin Winter[g,h], Robert Kostecki[b*]

a. School of Chemical Engineering at Sichuan University, Chengdu, 610065, China
b. Energy Storage & Distributed Resources Division, Lawrence Berkeley National Laboratory, 1 Cyclotron Road, Berkeley, CA, 94720, USA
c. College of Electrical Engineering at Sichuan University, Chengdu, 610065, China
d. Advanced Light Source, Lawrence Berkeley National Laboratory, Berkeley, California 94720, United States
e. State Key Laboratory for Physical Chemistry of Solid Surfaces, Department of Chemistry, College of Chemistry and Chemical Engineering, Xiamen University, Xiamen 361005, China
f. Department of Nanoengineering, University of California San Diego, La Jolla, CA, 92093, United States
g. MEET Battery Research Center, Institute of Physical Chemistry, University of Münster, Corrensstraße 46, 48149 Münster, Germany
h. Helmholtz Institute Münster – Forschungszentrum Jülich GmbH (IEK 12), Corrensstrasse 46, 48149 Münster, D-48149 Münster, Germany
i. Helmholtz Institute Ulm (HIU), Ulm 89081, Germany
j. Department of Chemical and Biomolecular Engineering, College of Chemistry, University of California, Berkeley, CA, 94720, United States
k. Neutron Scattering Division, Oak Ridge National Laboratory, Oak Ridge, TN, 37830, USA
l. Department of Energy, Politecnico di Milano, Via Lambruschini 4, Milano, 20156, Italy

[#] These authors made equal contributions
* Corresponding author

Abstract

Although the two active redox centers in Li-rich cathodes, including the anionic and cationic contributions, can enable Li-ion batteries to achieve outstanding specific energy, their behaviors at different current densities have not been clarified. Here, we provide a comparative study of the transition metals (*TMs*) and oxygen redox activities by directly accessing their oxidation states in Li-rich materials operated at very different current rates. Our data reveal the oxidation of oxygen in the near-surface region is at the same level for electrodes cycled with a wide range of current rates, indicating a reaction gradient of lattice oxygen redox reactions. The oxidation process of lattice oxygen is found to be dynamically compatible with that of the *TMs*. Combining the results of first principles calculations and complementary experimental findings, we propose a detailed mechanism of structural distortion from octahedral Li to tetrahedral Li and the role of oxygen vacancy in Li^+ diffusion. It is found that fast delithiation occurring at high current densities can easily cause local structural transformation, leading to a limited Li^+ diffusion rate and consequently suppressing rate capability.

Introduction

Layered transition metal oxides, commonly with the formula of $LiNi_xCo_yMn_zO_2$ (NCM, x+y+z=1), are currently used as cathode in Li-ion batteries (LIBs) for electric vehicles (EVs) and portable electronic devices due to their high average operation potentials of ≈3.6-3.8 V and high specific capacities of 150-220 mAh g^{-1}.[1] Lithium (Li)- and manganese (Mn)-rich layered oxides, $Li_{1+\alpha}Ni_x'Co_y'Mn_z'O_2$ (LMR-NCM, x'+y'+z'=1-α) offer very high reversible capacities (≈280 mAh g^{-1}) at a lower cost[2,3,4,5,6]. It has been widely accepted that both the transition metals (*TMs*) cations and the O^{2-} anions are involved in reversible redox processes in LMR-NCMs, contributing to the high capacity and energy density[7,8,9].

In all LIBs, the charge/discharge performance is primarily determined by the rate of lithium-ion diffusion and the kinetics of charge transfer during electrochemical processes[10,11]. In a battery of which the cathode remains the bottleneck of the capacity and energy density, the reactions can easily reach dynamic equilibrium state across the particle diameter of the electrode materials at *low* current densities, while the Li-ions within the particles will not reach a saturated state. However, if the current density is increased to a level that the Li^+ transport rate in the electrolytes surpasses that in the electrode materials, the charge transfer will occur primarily on the electrode surface with an overpotential induced by such a nonequilibrium condition. Consequently, inserted lithium will produce a concentration gradient between the surface and the bulk of an active material particle according to Fick's first law.[12]

The chemistry of the active material controls the kinetics of the charge transfer process, and most electrode materials face this significant limitation of charge/discharge rate capability. LMR-NCM materials were recognized to experience the sluggish oxidation reactions at the end of charge, which is attributed to the voltage range of oxygen oxidation (4.42 V-4.80 V) from previous studies.[13,14]. However, experimental results showed that materials without oxygen activity, such as $LiFePO_4$[15] and $LiMn_2O_4$[16], still suffer from the sluggish reactions near the end of the charge/discharge. Grey's group has thoroughly studied the sluggish reactions in the conventional NCM cathode via combining electrochemical methods, solid-state NMR and *operando* X-ray diffraction (XRD), and they demonstrated the relationship between the Li-ions diffusion coefficient and the local structural changes of NCM in the first cycle[17]. During the charging process, an increase in Li-ion mobility presents up to ~ 70% state of charge (SOC), together with an increase in the interlayer spacing and the creation of Li vacancies. Fast Li-ions hopping starts at 20% SOC and reaches a maximum of 40% to 50% SOCs. In the stage above 70% SOC, the overall layer spacing and corresponding unit cell volume collapse rapidly, which causes decreased Li-ion transport and sluggish diffusion in the oxygen-close-packing framework.[17] In the case of LMR-NCM materials, it was also reported that oxidation of the lattice oxygen, evolved gradually in the charging process from the near-surface region into the bulk, then triggering an undesired oxygen release and *TMs* migration, which resulted in an irreversible capacity loss and a low coulombic efficiency.[18,19] Since redox reactions at the *TM* cationic centers exhibit fast kinetics in comparison with the sluggish anions, which is

demonstrated by hard X-ray photoelectron spectroscopy (HAXPES) of Li-rich cathodes (*i.e.*, $Li_2Ru_{1-y}SnyO_3$[20] and Li-rich NCM[13]), the kinetics limitations for oxygen redox systems has remained one of the most critical challenges with regard to the fundamental understanding of the material operation and its practical applications[21]. Recent debates on oxygen redox reactions in LMR-NCM materials have led to significant advances in the characterization for direct probes of the oxidized oxygen in the material lattice. Conventional O-K spectroscopy has been widely employed on such topics; however, the application of X-ray Photoelectron Spectroscopy (XPS) has been seriously challenged by its probing depth and signal origin[22], and the X-ray Absorption Spectroscopy (XAS) pre-edge discussion has been linked entirely with *TMs* states[23]. On the other hand, high-efficiency mapping of resonant inelastic X-ray scattering (mRIXS) has been demonstrated to be a powerful tool for detecting the oxidized oxygen states in cathode materials for Li-ions and Na-ions batteries[24], as well as distinguishing the reversibility of active lattice oxygen in redox reaction[25]. By this time, such an advanced characterization techniques coupled with other electrochemical and structural probes, have not been used for a systematic exploration of the rate-dependent redox activities of cathode materials. In fact, most reports on anionic redox in LMR-NCM materials are limited to the investigation of charge-compensation at low current densities.[26,27]

In this work, we study transition metal and oxygen redox behavior in LMR- NCM using synchrotron-based sXAS and mRIXS methods, neutron powder diffraction (NPD) and density functional theory (DFT) modeling in composite electrodes cycled at high and low current density. The direct evidence of the same rate activation of oxygen, the tardy reaction of nickel, and the strong oxidation of oxygen in the bulk at a high rate provides new insights into the charge-transfer kinetics. Based on the experimental and simulation results, the poor rate capability and low coulombic efficiency has been correlated with the formation of tetrahedral Li sites due to the charge-compensation response for oxygen in the initial cycle, which blocks Li-ions diffusion in the corresponding electrochemical process.

Results

The Experimental section in the Supporting Information (SI) presents the synthesis of $Li_{1.2}Ni_{0.16}Co_{0.08}Mn_{0.56}O_2$ material and the electrode preparation. The SEM image of the LMR-NCM electrode, illustrated in Figure S1, shows spherical secondary particles of the active material ranging in size from 5-30 μm. During the electrochemical charge-discharge process, Li-ions can be reversibly extracted from or inserted into the Li-layer and the Li-*TM*s oxide frame of the LMR-NCM host material, corresponding with the oxidation or reduction of cations (*TMs*) and anion (oxygen), as shown in Figure 1a. The initial voltage profiles of LMR-NCM within an operating voltage window of 2.0-4.8 V at 0.1C and 10C (1C=250 mA g^{-1}) are shown in Figures 1b and 1c, respectively. The corresponding gas release (predominantly oxygen and carbon dioxide, with carbon monoxide also evolving in very minor quantities not shown[28] during the charging process, determined by operando differential electrochemical mass spectrometry (DEMS) [29]at 0.1C and at 10C, are shown in Figures 1d and 1e. At 0.1C, the voltage profile (Figure 1b) starts as an S-

shape slop from pristine state to 4.42V, followed by a characteristic long plateau (until reaching 4.65V) and a short rapid increase to the end of the first charge process (4.80V). In contrast to the cell cycled at 0.1C, which displays a relatively long plateau, the one cycled at 10C shows an obvious overvoltage, postponed end of the slope and a shortened plateau from 4.65V to 4.80V. Such a clear electrochemical contrast provides a unique opportunity to clarify the oxygen activities of the activation process at different current densities and its influence on the poor rate performance of LMR-NCM materials.

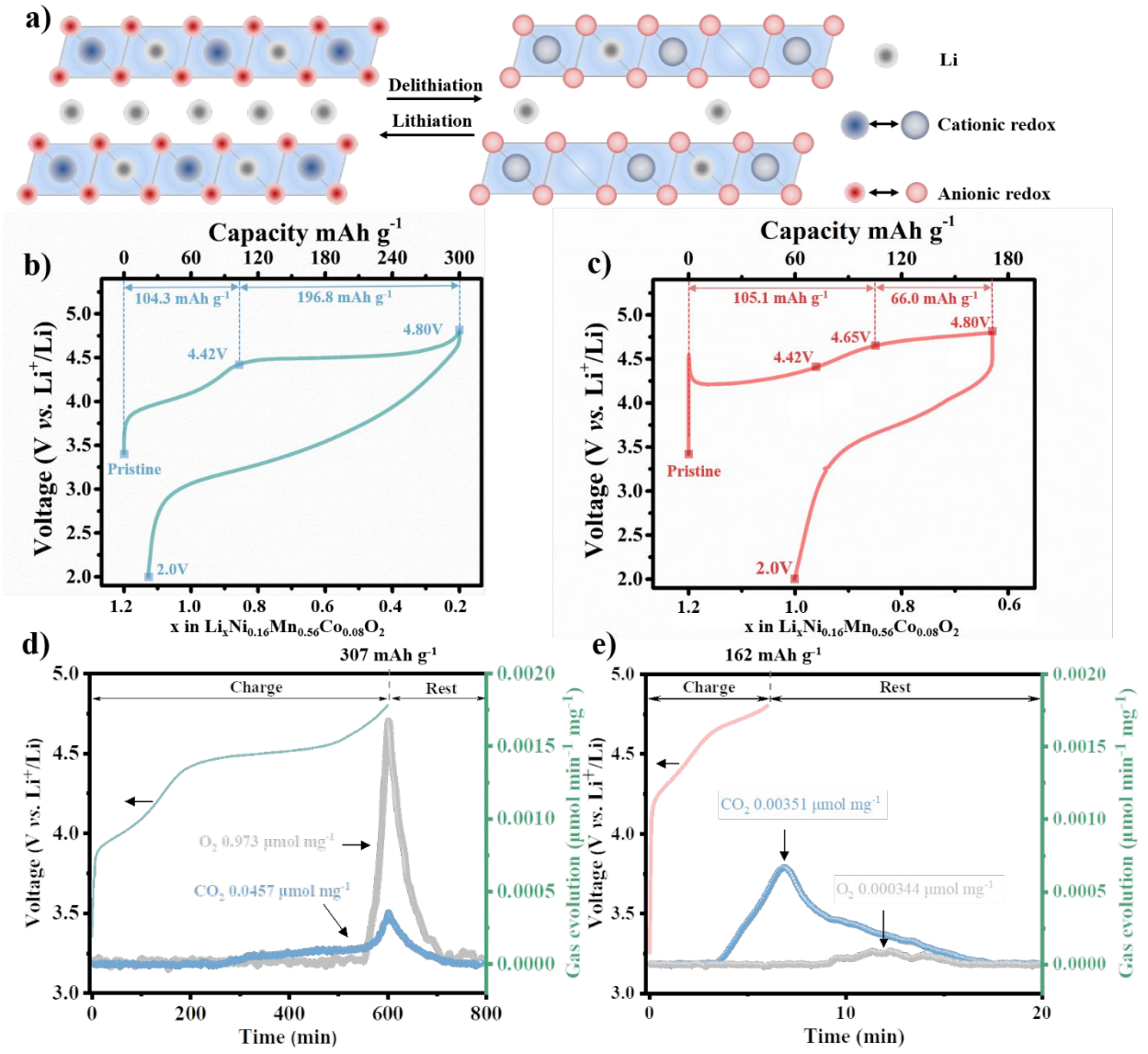

Figure 1. Illustration of the charge compensation and Li-ions diffusion of LMR-NCM during the redox process (a); the corresponding voltage profiles of $Li_{1.2}Ni_{0.16}Co_{0.08}Mn_{0.56}O_2$ material charged and discharged at 0.1C (b) and 10C (c); the O_2 and CO_2 evolution for electrodes charged at 0.1C (d) and 10C (e), respectively.

As shown in the initial charge profile at 0.1C, the slope completes at 4.42V, which is a clear sign for the

full oxidation of *TMs* (Ni and Co).[30] The electrode cycled with high current density (10C) displays a short slope starting from 4.42V. Characterizing the oxidation state of the involved cations and anion at 4.65V can explain this significant change of electrochemical profile. Although a small amount of CO_2 gas release can be still observed from the time delayed gas spectra which associated with fast electrochemical process, only a negligible oxygen release can be detected. Given that most of the oxygen release occurs at the end of the charging process (corresponding to a voltage above 4.65V) at a low current rate (as shown in Figure 1d, and consistent with prior studies[28,29,31,32]), the higher voltage plateau observed for the Li-rich cathode charged at 10C is mainly contributed by the oxidation of lattice oxygen, but it does not reach the oxygen release stage due to the overvoltage and poor kinetic for oxygen gas generation at high voltage. Upon the discharge process, both profiles show clear S-shape features but present quite different scopes.

A series of electrodes at different SOCs (at the voltages marked in Figures 1b and 1c) were studied by sXAS and mRIXS measurements. *TM*s (Mn, Co, and Ni) *L*-edge sXAS were measured in two detection modes for this study, *i.e.*, the total electron yield (TEY) and total fluorescence yield (TFY) with detect depths of 2-5 nm and 50 nm, respectively. The sXAS *L*-edge spectra of the *TM*s at different valence states have identical shapes, peak position, and normalized $L_{2,3}$ intensities (*e.g.*, the spectra for MnO, Mn_2O_3, and MnO_2 as reference spectra of Mn^{2+}, Mn^{3+}, and Mn^{4+} ions, shown in Figure S2; the calculated spectra for Ni^{2+}, Ni^{3+}, and Ni^{4+} collected from reference[33]). They could be used to quantify the proportion of each valence state based on a simple linear combination of the distinct line shape of *TMs* references for the covalent hybrid *ex-situ* sample.[34,35] The identified specific spectra are fitted for the experimental spectrum and then provide an ensemble-averaged oxidation state of the corresponding *TM* with high accuracy. The TEY and TFY spectra of *TM*s under selected SOCs are plotted in Figures 2**a-c** and 2**e-g** for direct comparison of the surface and bulk states. The corresponding mean valence states with quantitative contrast of surface and bulk are summarized in Figures 2d and 2h, respectively.

The spectra of *TMs* at the pristine state show no substantial differences between the TEY and TFY modes, except for a minor distortion of the Mn due to self-absorption.[36] When the electrode is charged to 4.42V at 0.1C, the peak shape of the Mn *L*-edge (Figure 2a) changes slightly compared to the pristine state. Since most Mn-ions exist as 4^+ in Li-Mn-rich material and only a small amount of Mn^{3+} presents,[35] the slight change mainly relates to the oxidation of Mn-ions. The peak position of Co *L*-edge (Figure 2b) shifts to higher energy, which can be observed from spectra in both TEY and TFY modes.[8] The Ni *L*-edge spectra (Figure 2c) indicate an obvious transformation from 2^+ to a higher oxidation state. Distinct from the consistent changes for the surface and bulk spectra of Co and Mn, the Ni *L*-edge spectrum in TFY mode appeared at higher energy values compared to its spectrum in TEY mode. Based on the reported Ni *L*-edge sXAS spectra[36] and the calculated mean valence state (shown in Figure 2d), it can be concluded that the oxidation state of Ni is higher in bulk than the surface at 4.42V. In an electronic description, Ni-ions on the

surface are fully or partially in a $d^7\underline{L}$ configuration due to the charge transfer of the type $d^n \rightarrow d^{n+1}\underline{L}$, where $\underline{L}$ denoted a positive hole in the oxygen valence band.[34] Therefore, the Ni-ions at the surface are not totally oxidized. As the electrode potential reached 4.8V, no obvious changes were observed when compared with spectra at 4.42 V, indicating that no further oxidation of *TMs* occurred during the long voltage plateau range.

Significant differences in the Mn *L*-edge spectra are seen in the discharged sample; Mn^{4+} is reduced to Mn^{2+}, particularly on the surface. In addition, a low-energy shoulder appeared in the Co *L*-edge spectra. Besides the oxygen loss shown in Figure 1d, the reduction of Mn and irreversible redox of Co clearly demonstrate a phase reconstruction occurred at 0.1C.

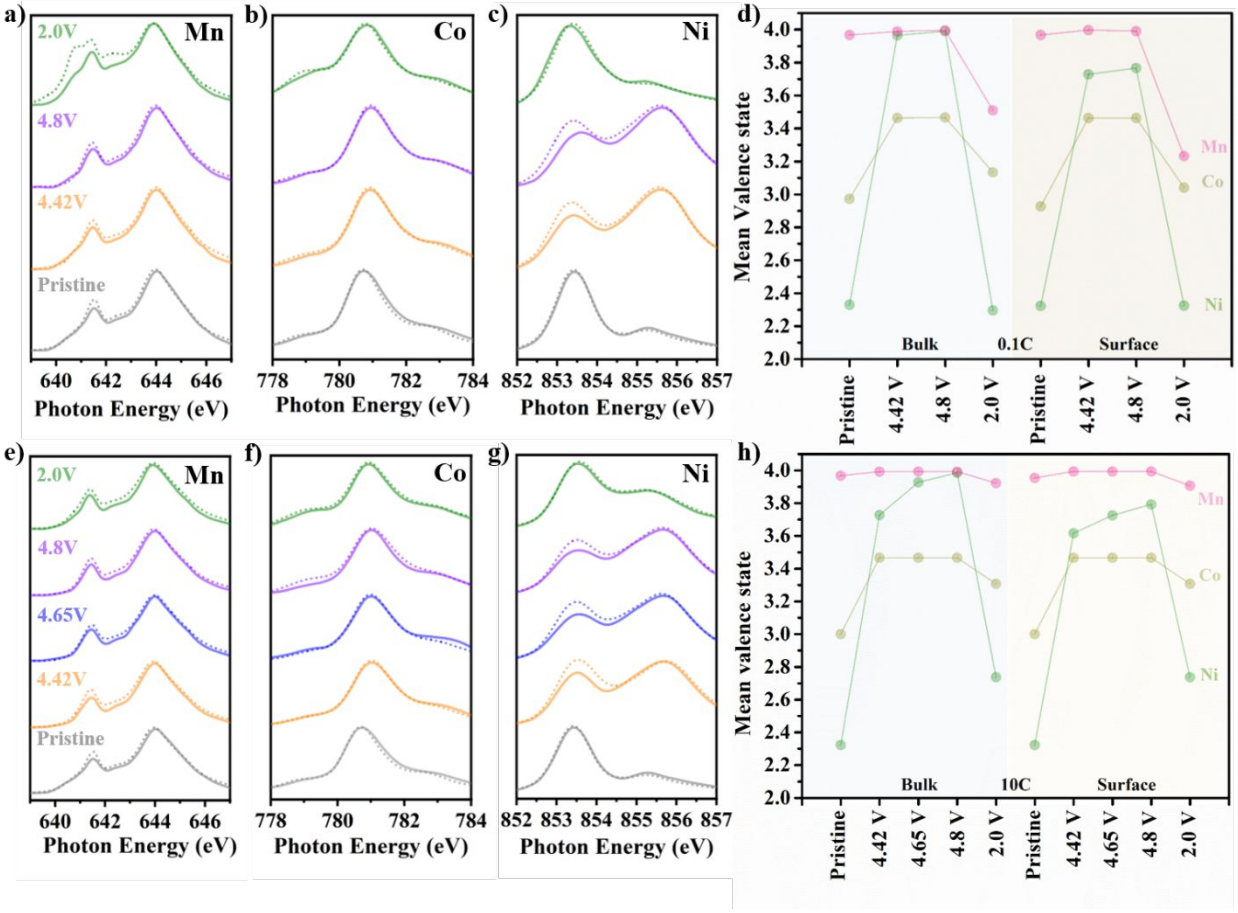

Figure 2. The *TMs* (Mn, Co, Ni) -L_3 TFY (solid line) and TEY (dash line) spectra with the bulk and surface valence states of electrodes are shown at representative SOCs during the initial cycle at 0.1C (2a-c) and 10C (2e-g) as indicated in Figure 1b and 1c, respectively. Figures 2d and 2h present the quantified mean oxidation states of each *TM*, based on the fitting results of the valence distributions in the spectra.

The resulting *TMs* spectra show similar trends for the electrode charged at 0.1C/10C, *i.e.,* Mn valence state remains constant value and Co is fully oxidized at 4.42V. Different from the electrode charged at 0.1C, in

which the oxidation of Ni is maximized at 4.42V (Figure 2g), a further increase of Ni valence state can be observed at 4.65V and 4.8V when it is charged at 10C from the calculated mean valence state (Figure 2h). This suggests tardy oxidation of Ni at high current density, where the non-equilibrium process is affected by charge transfer in the crystal structure. After the cell was discharged to 2.0V at 10C, neither Co nor Ni returned to their initial states. The redox reversibility is 59.8% for Ni and 34.1% for Co, which results in a low coulombic efficiency shown in Figure 1c. Even though Ni is continuously oxidized till the end of charge, the extra driving force of the motion of Li ions at a high charging rate can cause highly inhomogeneous Li-ions distribution and structural defects within the particles.

Figure S3 shows the TEY and TFY mode for O *K*-edge sXAS of LMR-NCM electrodes charged/discharged at 0.1C and 10C, respectively, measured in the TFY mode, revealing the electronic state evolution of oxygen in bulk. Although there are some general lineshape variation of the O-K pre-edge here (grey box), the O-*K* sXAS pre-edge is dominated by the *TM*-O hybridization, and the lineshape change is mostly due to TM and the hybridization state variations upon electrochemical states[23]. We, therefore, seek a more reliable probe and analysis of the oxygen redox state through O-K mRIXS, which has been demonstrated to be a superior technique to distinguish the oxidized states of lattice oxygen from the strong *TM*-O hybridization features in battery cathode materials[24,37]

Figure 3 presents the mRIXS results of all the representative LMR-NCM electrodes at different SOC as they evolve during the initial cycle. The pristine sample is characterized by broad features at around 525 eV emission energy, due to the *TM*-O hybridization in typical *TM* oxides.[38] These features get broadened in line shape and enhanced in intensity upon charge and behave inversely during discharge, which is consistent with the sXAS observation in Figure S3. During the initial charge to 4.8 V, the oxidized oxygen feature appears around 531.0 eV excitation energy (dot-box) and 523.7 eV emission energy (red arrow) in Figure 3a, which has been seen in various oxidized oxygen reference species[39,40]. We note that the emergence of this fingerprinting feature of lattice oxidized oxygen has been previously reported and analyzed in details for delithiated LMR-NCM electrodes prepared with low current densities.[27,24] Thus, the appearance of this feature and its disappearance indicate the reversible oxygen redox reaction in Li-rich compounds, which is consistent with previous reports[24,27,39,40].

The comparison of the LMR-NCM electrodes cycled at 0.1C/10C rate shows that there is negligible contrast on the oxygen redox behaviors between the electrodes cycled with 0.1C and 10C rates, i.e., both electrodes display no oxidized oxygen feature until above 4.42 V, and strong oxidized oxygen feature at 4.8 V, then reversibly disappeared feature when discharged (Figure 3a). To obtain more quantitative evidence, we extracted the super-particle fluorescence yield signals (sPFY) from the mRIXS maps by integrating the RIXS signals across the 523-524 eV emission energy window (dotted lines in Figure 3a). The mRIXS-sPFY is displayed in Figure 3b with the peak at around 531 eV (along x axis in emission energy),

representing the evolution of the oxidized oxygen mRIXS feature intensity upon different electrochemical states. The full intensity of the oxidized oxygen feature could be quantified by an area integration within 531±0.3 eV excitation energy in the sPFY profiles. (See the Experimental section in SI). The peak area evolution is plotted together with the electrochemical profiles in Figure 3c and Table S1. As shown in both the raw mRIXS data plots of Figure 3a and the extracted data of Figure 3c, the oxidized oxygen feature starts to emerge after 4.42 V in for both the 0.1C and 10C cycled electrodes. It is intriguing to observe that at, although 4.65 V is the starting point of the plateau of the 10C cycled electrode (Figure 1c), there is already a clear signature of oxidized oxygen of the 10C cycled sample at 4.65 V (red arrows in Figure 3a), indicating that lattice oxygen oxidation takes place before the voltage plateau during high rate cycling and is not really associated with the high voltage plateau in Li-rich compounds, as also suggested in previous studies[37]. In both cases, the oxidized oxygen becomes very strong in mRIXS results at the fully charged states. After the discharge to 2.0 V, the sPFY peak area for the two sets declines but is not restored to the pristine state, especially for the 10C set. Consequently, the reversibility of sPFY 531 eV area evolution during charge/discharge for 0.1C and 10C is 77.3% and 64.4%, respectively.

It is important to note that, although mRIXS detects the non-surface signals of the lattice oxidized oxygen, as verified through the comparison with microscopic results[27], it has a probe depth over hundred nanometers for O-K that is much less than the particle size of several micrometers. Therefore, the observation of the same level of oxidized oxygen states in 0.1C and 10C electrodes indicates that the oxygen redox takes place with a reaction gradient or reaction heterogeneity, with likely oxidized oxygen first taking place in the near-surface region (about 100-200 nm near the surface). Although this is bulky considering the lattice parameters of the surface regime, it is still a near surface region compared with the particle size. Additionally, oxidized oxygen during the initial charging of Li-rich compounds may involve other reactions than lattice oxygen redox, e.g., oxygen release and strong surface reactions[42]. Because RIXS detects only the lattice oxidized oxygen that is maintained in the lattice, in another word, the part that is most likely reversible., the mRIXS observation here suggest that, with the possible reaction gradient of the oxygen redox, the oxidized oxygen in the near surface region remains the same for the 0.1C and 10C charged electrodes. The observation of the same level of oxidized oxygen does not conflict with the overall electrochemical capacity differences under different rates, which are likely due to other oxygen oxidation reactions. The fundamental reaction mechanism of oxygen redox is still under debates, it has been found that the reaction takes place based on a typical core-shell models[41]. Therefore, considering all the 3 factors, i.e., the mRIXS detects the near surface region, lattice oxygen oxidation is only part of the oxidation process, and the oxygen redox reaction takes place from the near surface region and migrates into the core of the particle, it is actually not surprising to observe the same level of oxygen oxidation by mRIXS. Nonetheless, it is intriguing that the near-surface oxidized oxygen seemingly remains almost identical for electrodes

cycled under rates with 100 times difference, which could be an interesting topic for future theoretical studies.

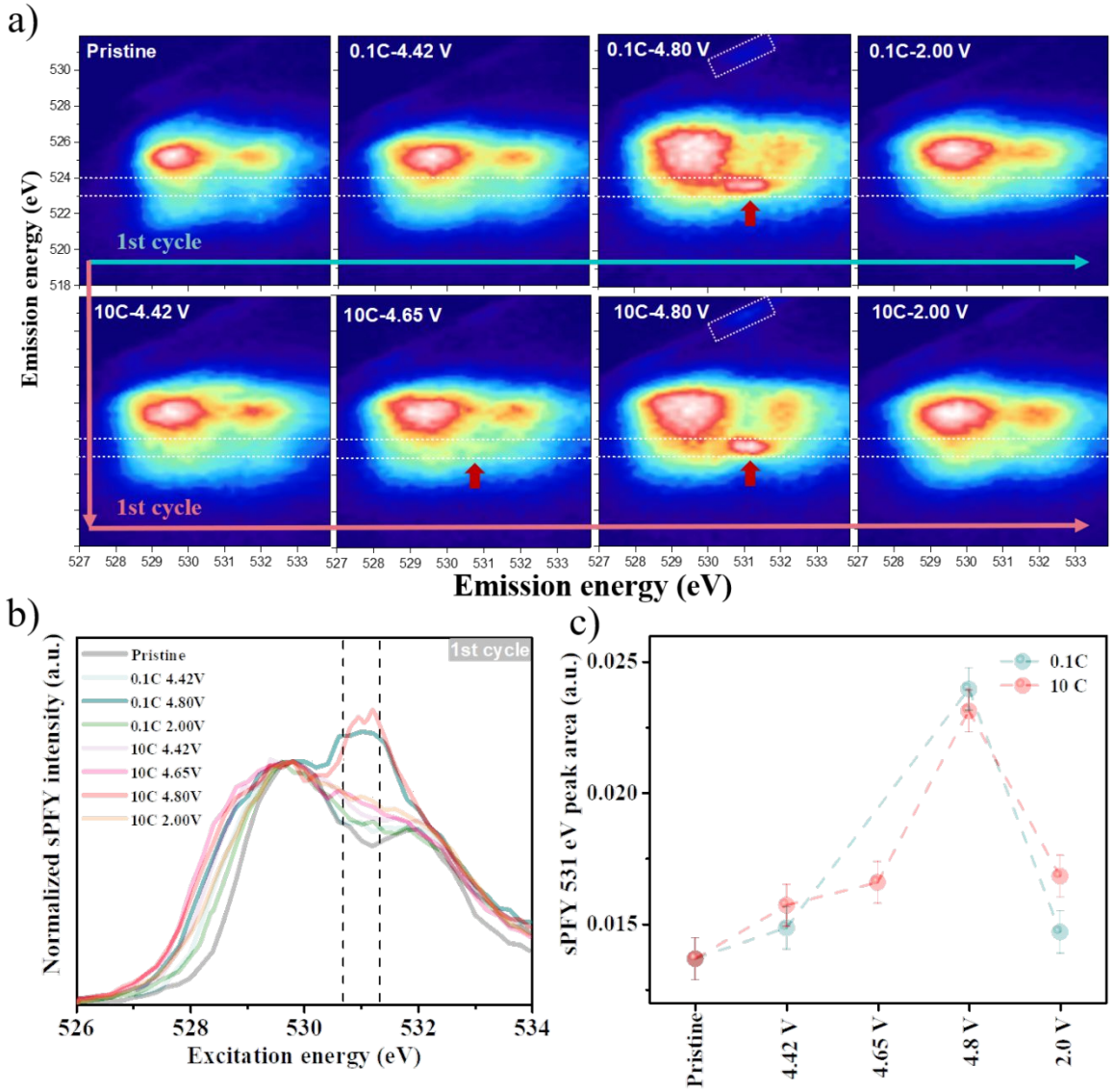

Figure 3. a) The mRIXS mapping of all the representative LMR-NCM electrodes at different SOCs in the initial cycle. b) The corresponding sPFY profiles extracted from the emission energy window in the range of 530.7-531.3 eV. c) The peak area evolution of the oxygen oxidation at 0.1C and 10C.

From the sXAS and mRIXS-sPFY results, we addressed some important questions from the comparison between the 0.1C and 10C sets. First, we have fingerprinted the charge-compensation mechanism of cationic and anionic redox at both low and high rates. This distinguishes the rate dependent contribution of *TMs* and O on delivered capacity. Second, we provided direct spectroscopic proof of the influence of cationic and anionic redox on overvoltage. The differential capacity (*vs.* voltage, dQ/dV) profiles of LMR-NCM electrodes during the charging process and their corresponding reaction rates of *TMs* and O (calculated based on the oxidation states)[43], as

shown in Figure S4, demonstrate that both the cathodic and anionic reaction at 10C has a strong effect on overvoltage. However, this different behavior at high current density may be associated with a different kind of *TM*-O hybridization on charge-compensation or with the effect of structural changes on lithium-ions diffusion. It worth mentioning that, at high dis-/charge rate, oxygen is activated below the high voltage plateau, as discussed above.

To gain deeper insight and understanding of the mechanism of the structural changes, especially for oxygen and Li, the LMR-NCM electrodes at different SOCs were investigated using NPD.[44] The refinement patterns and the corresponding results for LMR-NCM at pristine state (Figure S6 and Table S2), fully charged state (4.8V) at 0.1C (Figure S7 and Table S3) and 10C(Figure S8 and Table S4), fully discharge state (2.0V) at 0.1C (Figure S9 and Table S5) and 10C (Figure S10 and Table S6) are displayed in the supporting information. The refined lattice parameters *a* and *c* are plotted in Figures 4a and 4b, respectively. During the charge process, delithation together with the increase of valence states of Ni^{2+} and Co^{3+} results in a drop of the *a* lattice parameter due to the decrease of ionic radii of *TM*s (*e.g.*, r Ni^{2+} = 0.69 Å, r Ni^{3+} = 0.60 Å, r Ni^{4+} = 0.48 Å).[45] The smaller change to the *a* lattice parameter at 10C is caused by the oxidation of the lower proportion of *TM* ions. At the end of the discharge process, the *a* lattice parameter of the sample discharged at 0.1C has increased to a higher value than in the pristine state, due to the additional reduction of Mn ions. The sample discharged at 10C has a slightly decreased *a* value than in pristine material because the valences of Ni and Co ions are not fully reduced to their pristine states. In contrast, the removal of Li-ions at 0.1C and 10C induces a different change trend from *c* lattice parameter, *i.e.*, an increased *c* value, in terms of the charge at 10C, is caused by a concentration gradient and electrostatic repulsion from adjacent oxygen layers;[46] while with many more Li-ions extracted at the charged state, as in the case of 0.1C, the *c* lattice parameter value decreased even below the pristine state. As Li-ions were inserted back into the host structure, though cycled at different current rates, the *c* lattice parameters change back and reach a similar value that is higher than the original state.

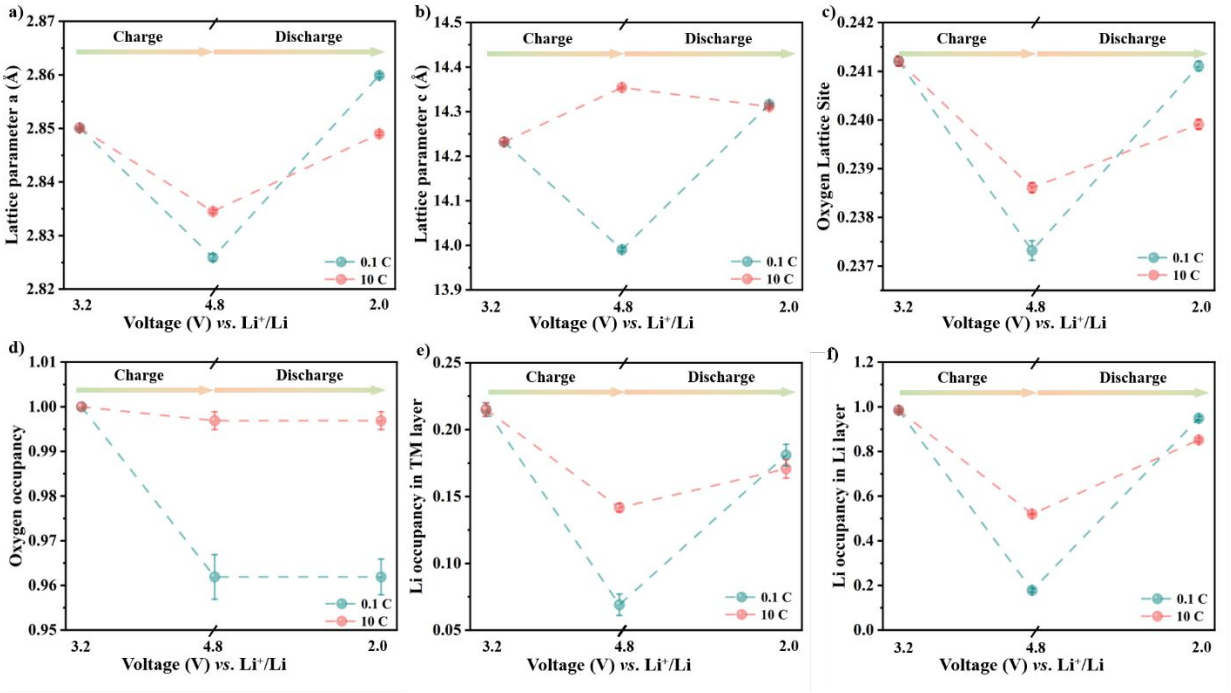

Figure 4. The refinement results from the fully charged/discharged states at 0.1C and 10C with error bar: a) the *a* lattice parameter, b) the *c* lattice parameter, c) oxygen lattice site, d) oxygen occupancy, e) Li occupancy in TM layer, f) Li occupancy in Li layer.

Figure 4c plots the refined oxygen positions. During the charging process, the oxidation of *TMs* increases the electrostatic attraction between the *TM* ions and oxygen ions, thus resulting in a shortened *TM*-O bond, which is consistent with the changes of the *a* lattice parameter. However, in contrast to the sample cycled at 0.1C, in the sample cycled at 10C, the oxygen position is unable to return to its original state. This suggests that significant Li-ion diffusion over a short period caused a highly irreversible structure distortion at the end of discharge. As illustrated in Figure 1a, two different lithium sites are located in the Li-rich layered oxide host. The Li-ions in the *TM*s-oxide layer are edge-sharing with three octahedral Li-ions (Li_{oct}) in the adjacent Li-layer. However, the energy of removing one Li per cell from the Li layer is lower than that from the *TM* layer. If the edge-sharing Li_{oct} ions are extracted, a Li ion will migrate from the octahedral site into the tetrahedral site, face-sharing with Li in the *TM* layer. The shortage of active Li-ions in certain regions may cause irregular ionic diffusion, some of the Li-ions to be extracted from the *TM*s-oxide layer at lower potential, and leads to the formation of tetrahedral Li (Li_{tet}). Therefore, as mentioned in the mRIXS result, close to 26% of lattice oxygen is oxidized below 4.42V when charged at 10C. This activation is below the oxidation potential of oxygen to compensate the charge transfer. This charge compensation process sacrificed the reversible changes of the oxygen lattice site and instead caused crystal distortion. The changes to oxygen occupancy demonstrated the oxygen release during the electrochemical process. As shown in Figure 4d, the decrease of oxygen occupancy indicates a clear oxygen loss (with O_2 gas release), which only occurs for the sample charged at 0.1C. The changes in oxygen occupancy

are consistent with the operando DEMS results shown in Figures 1d and 1e.

The refined Li occupancy in both *TMs* and Li layers (shown in Figures 4e and 4f) proves that most of the Li-ions are located at the Li-layer, while the rest of Li-ions stay within the *TMs* oxide frame at pristine state. Li-ions in both the Li-layer and the *TMs* layer participate in the electrochemical process independent to the rate applied. However, the transfer of Ni-ions to Li-layer shows different behavior at 0.1C and 10C, as displayed in Figure S5. With the appearance of a higher amount of oxygen vacancy when charged at 0.1C, the Li/Ni mixture becomes served at the end of the charging process. In the case of high current density, no obvious Li/Ni mixture changes with no occurrence of oxygen release. Besides the migration of *TM*s-ions to Li-layer, it has been reported that the appearance of Li_{tet} blocks the Li-ions inserted back into the original sites.[47,48] Hence, the much smaller amount of Li-ions re-inserted at 10C, indicates the strong blocking effect of tetrahedral Li at high current. Only 24% of Li-ions in the *TMs* layer (Figure 4e) can be reversibly inserted at the end of the first discharge. In addition, it also influences the reversibility of Li-ions in the Li-layer. Such poor reversibility is consistent with the low coulombic efficiency for the first cycle.

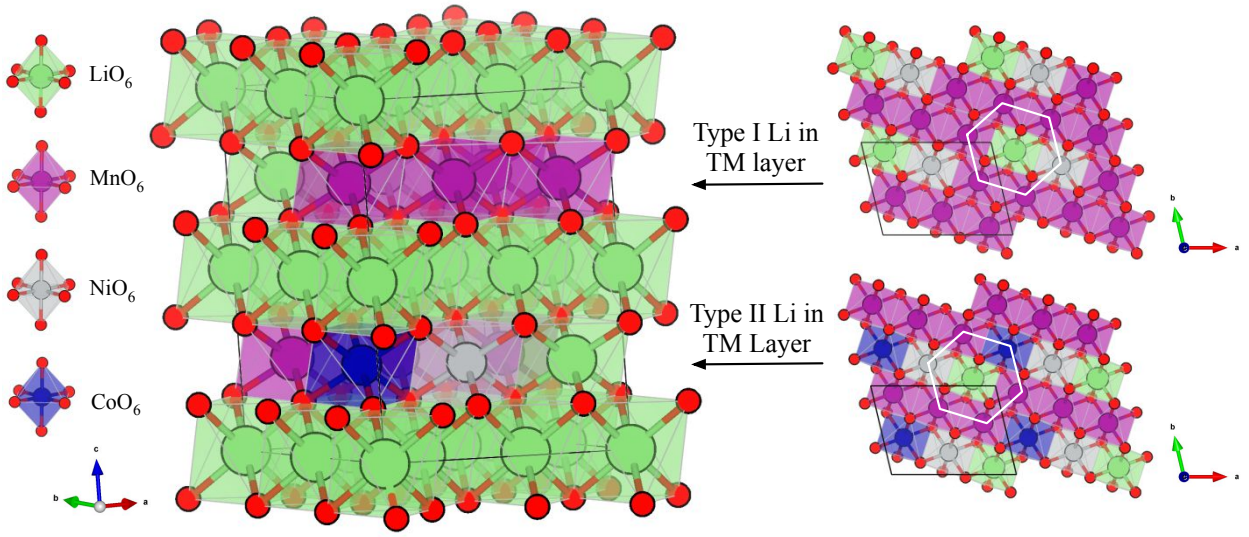

Figure. 5 The ground-state structure of 3 × 2 × 2 supercell of $Li_{1.2}Ni_{0.16}Co_{0.08}Mn_{0.56}O_2$ and the top views of cation ordering patterns in *TM* layer from DFT calculations.

To elucidate the diffusion mechanism in different charge-discharge rates (0.1C or 10C) in conjunction with neutron powder diffraction, we performed density functional theory (DFT) calculations using PBE+*U* functional in 3 × 2 × 2 supercells of layered Li*TM*O_2 primitive cell (space group: *R*-3*m*) containing 12 formula units. Li ions can reside in the Li and *TM* layers of close-packed oxygen frameworks, typical from layered oxides of ABCABC stacking (O3-type). The supercells of $Li_{14}Ni_2CoMn_7O_{24}$ ($Li[Li_{2/12}Ni_{2/12}Co_{1/12}Mn_{7/12}]O_2$), roughly equivalent to pristine $Li[Li_{0.2}Ni_{0.16}Co_{0.08}Mn_{0.56}]O_2$, were set with the occupancies as Li:Ni:Co:Mn = 2:2:1:7 in the *TM* layer and Li fully occupied in Li layer at octahedral sites. The cation orderings in the *TM* layer have a substantial effect on the energy of this system. To more efficiently

explore possible cation orderings, we applied MEGNET[49] deep learning package to energetically rank the orderings and thereby reduce the structures subsequently calculated with DFT. The DFT-relaxed energies are in excellent linear relation with the MEGNET predicted ones for 100 random orderings as shown in Figure S11. We performed the MEGNET-based energy prediction screening among all >1000 structures and finally, a structural relaxation was applied to those with predicted E_{hull} < 5 meV/atom.

From the obtained ground-state configuration (see Figure 5), two distinct Li local environments in the *TMs* layer were found, and they are categorized by their surrounding *TM*s: (1) type I Li surrounded by 5 Mn^{4+} and 1 Ni^{2+}; and (2) type II Li surrounded by 4Mn^{4+}, 1 Ni^{2+} and 1 Co^{3+}. The oxidation states of those *TM*s from calculations are consistent with the experimental results in Figures 2d and 2h. The oxygen vacancies start to be formed in the plateau region (4.42-4.8V) at 0.1C rate (Li content ~0.83)[46] and finally reach the concentration of 4% O_2 release as detected by the refined XRD at the end of the charging process (4.8V). To mimic that state, we extracted (i) 4/12 Li ions in the Li layer and (ii) 2/48 distinct oxygen ions sequentially from the pristine $Li_{1.2}Ni_{0.16}Co_{0.08}Mn_{0.56}O_2$ for the following calculations. For the high charging rate (10C) process, it leads to <0.5% oxygen loss (Figure 1e), which is lower than can be accommodated with the 48 oxygen atoms in the supercell and not reflected in the calculation.

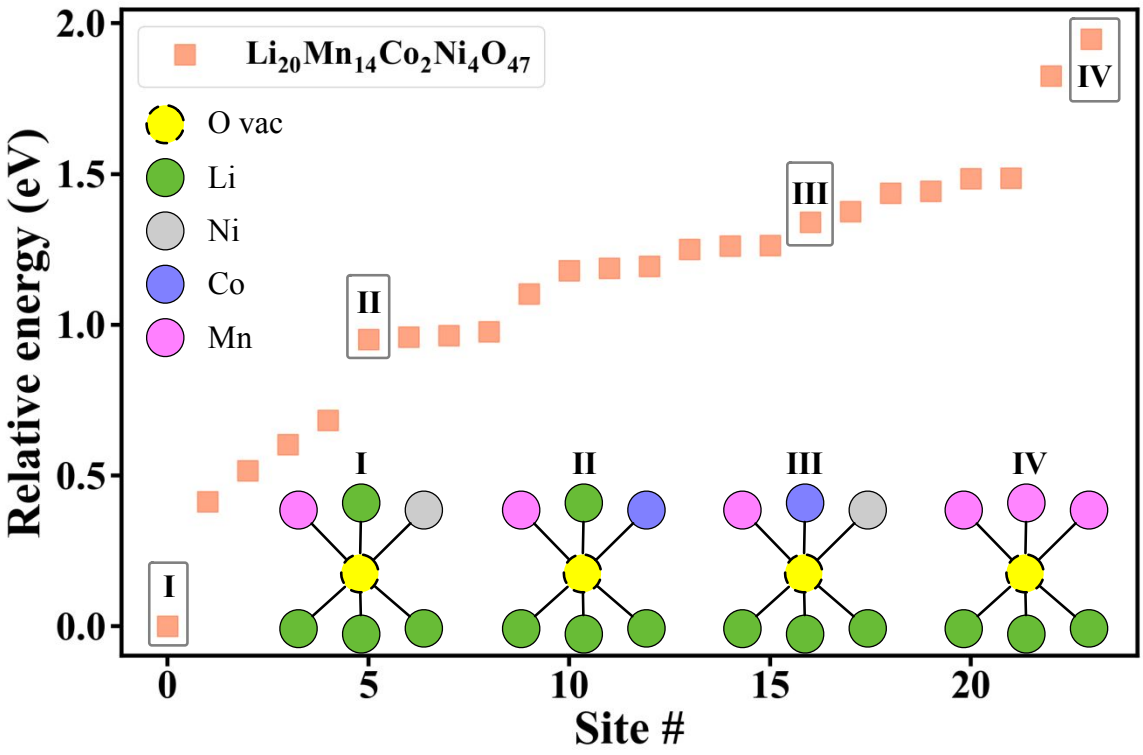

Figure 6. The relative energies of oxygen vacancy in different local environments. The 24 distinct oxygen vacancy sites in $Li_{0.83}Ni_{0.16}Mn_{0.56}Co_{0.08}O_{1.96}$ are sorted by increasing site energy. Four examples of local environments are given and labeled from type I to IV. The relative site energy of oxygen vacancy is highly dependent on its nearest neighbors in the *TM* layer: I [Li, Ni, Mn] < II [Li, Co, Mn] < III [Ni, Co,

Mn] < IV [Mn, Mn, Mn]. We note that these energies are roughly in-line with what would be expected from electrostatics; *i.e.*, Li (1+) neighbors are the most preferred and Mn (4+) neighbors are least preferred.

In the pristine LMR-NCM structure, each oxygen ion is fully coordinated with 6 cations (Li or *TM*). As the charging process proceeds, Li ions are extracted from the Li layers and the cation coordination number of oxygen ions is reduced to 5 or 4 with Li vacancies in Li layer. We compared the energies of the symmetrically distinct oxygen sites and found that it is most likely for the oxygen vacancy to form when its *TMs* layer combination is Li-Ni-Mn as shown in Figure 6, which is in good agreement with previous studies.[50] The oxygen vacancy (Kroger notation: $V_O^{\bullet\bullet}$), which exhibits positive charges, should be more stable with less positive charges. Thus, the electrostatic repulsions between the oxygen vacancy and other cations increase by order of Li < Ni < Co < Mn, which results in the type IV oxygen vacancy (coordinated with 3 Mn^{4+} in the *TM* layer) having an ~ 2 eV higher energy than type I (coordinated with Li^+, Ni^{3+}, Mn^{4+} in the *TMs* layer) as shown in Figure 6.

To study the influence of oxygen defects in the Li-ion migrations, we selected a stage of discharge at $Li_{20/28}$ concentration (unit cell formula: $Li_{0.83}Ni_{0.16}Co_{0.08}Mn_{0.56}O_2$) to simulate using first-principles nudged-elastic band (NEB) calculations. This stage is generally acknowledged as a rate-determining step for Li-rich layered oxides.[51] During this stage, the Li-ion hops from one octahedral site of the Li layer into another octahedral site through the intermediate tetrahedral site, which is face-shared with a cation in the *TMs* layer (see Figure 7). This type of *o-t-o* paths are well-known in layered $LiMO_2$ cathodes.[52] When no oxygen vacancy is introduced (10C rate), the Li migration barriers we calculated based on the ground-state $Li_{0.83}Ni_{0.16}Co_{0.08}Mn_{0.56}O_2$ are 256 meV, 272 meV, and 447 meV for *TM*s=Ni, Co, Mn, respectively. The Li tetrahedral site, which is face-shared with the *TMs* layer Li, is relatively stable. Thus, we also observed spontaneously formed Li_{tet} in the Li layer in conjunction with the main *o-t*(*TM*)*-o* hopping from the NEB calculations. Once a Li-ion is trapped to those low-energy tetrahedral sites (face-shared with Li in *TMs* layer), it forms a "Li-Li dumbbell" that prevents Li from further diffusing into adjacent octahedral sites in the *TMs* layer.[48] These Li-Li dumbbells block long-term Li diffusion and reduce the reversible capacity at a 10C rate. The poor performance of 10C rate can be attributed to such tetrahedral Li trapping (face-sharing with 2/12 Li in *TMs* layer) and high *o-t(TM)-o* barriers (7/12 *TM*=Mn in *TMs* layer) assuming a complete random cation ordering in *TMs* layer.

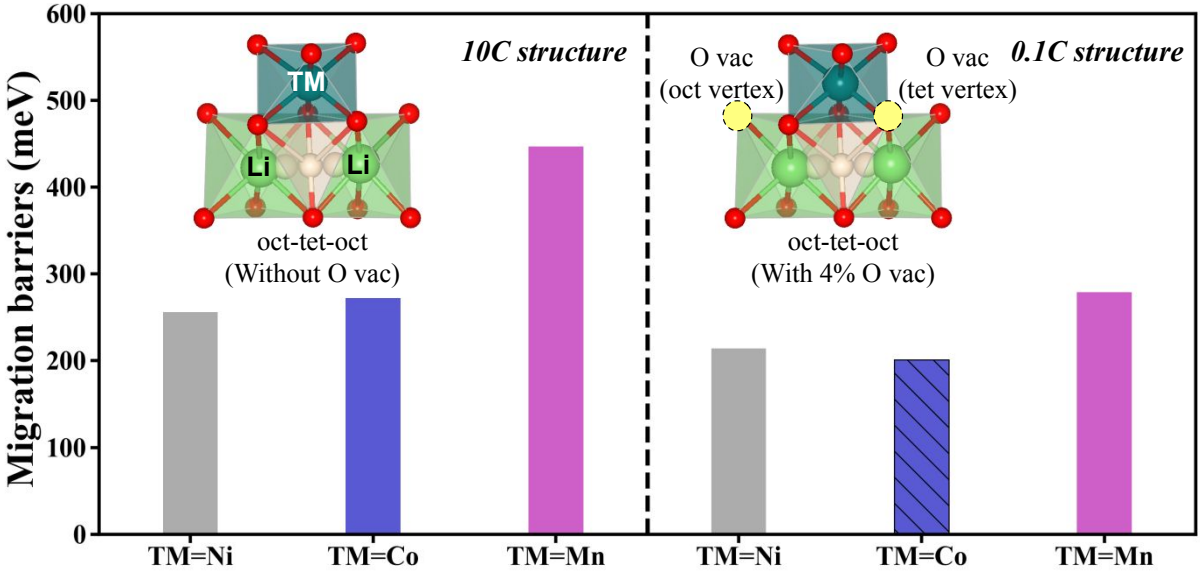

Figure 7. Li^+ migration barriers for *o-t-o* pathways in $Li_{0.83}Ni_{0.16}Mn_{0.56}Co_{0.08}O_{2-\sigma}$ with and without oxygen vacancy. At 10C rate (left part, without oxygen vacancy), over. The barriers are 256 meV, 272 meV, and 447 meV for *TM*=Ni, Co, Mn, respectively. After introducing a 4% oxygen vacancy (right part, 0.1C structure), the migration barriers are reduced by 40-170 meV depending on the *TMs* species and the arrangements of vacancies (*e.g.*, divacancy distance). The major influences on migration barriers are from the primary oxygen vacancies, which are either seated on the vertex of LiO_6 octahedron (oct vertex) or the vertex of the intermediate LiO_4 tetrahedron (tet vertex), as shown here. It is unlikely that two oxygen vacancies sit in the same TMO_6 octahedron due to the strong repulsion in such a small distance. The hatched bar for *TM*=Co means there is no primary oxygen vacancy found in the path(s) we calculated.

When 2/48 oxygen vacancies are introduced at 0.1C rate, factors like trapped Li-Li dumbbells and high barriers for *o-t(Mn)-o* which degrade the Li conductivity and rate performance are eliminated. From our DFT calculations, it is unlikely that two oxygen vacancies can sit in the same TMO_6 octahedron due to the strong repulsions in such a small distance. As a representative, we used 2 reasonably low-energy configurations (divacancy distance = 3.1Å or 5.8Å) to simulate 5 distinct paths and labeled each path whether the O vacancy is primary (in the oct/tet vertex of LiO_6/LiO_4) or secondary (not in any oct/tet vertex of the *o-t-o* path) in Figure S12. Compared with the 10C case, the oxygen vacancies facilitate Li diffusion in LMR-NCM in two ways: (i) The under-coordinated tetrahedral site face-shared with Li in the *TMs* layer is no longer stable due to the $V_O^{\bullet\bullet} - Li^+$ repulsion. Even if trapped, the Li ions have a higher rate of escaping from the tetrahedral sites and can continue to diffuse. Such a low Li_{tet} rate at low current densities (0.1C) could help to relieve the diffusion-block issue. (ii) The overall migration barriers for *o-t-o* paths are significantly reduced by 40-170 meV as shown in Figure 7. For 7/12 *o-t(Mn)-o* paths, it suffers a high barrier of 447 meV and from our calculations, primary O vacancy with a short divacancy distance of 3.1Å can reduce it to 202 meV.

Although the location of oxygen vacancy and divacancy distance have their complicated effect on reducing the Li migration barriers, the majority issues (theoretically ~2/12 Li-Li dumbbell blocking and ~7/12 high *o-t(Mn)-o* barriers) are solved by the existence of oxygen vacancies.

Conclusions

In summary, our combined chemical, structural and theoretical studies on LMR-NCM at different current densities have demonstrated the reason for the low first-cycle Coulombic efficiency at high current densities and the poor-rate performance. The detailed spectroscopic data reveal an intriguing reaction gradient of the oxygen redox activities, with a surface of oxidized oxygen state of the electrode particles cycled at a high rate at the same level as that cycled with 100 lower rates. Moreover, quantitative tracking of the cationic and anionic redox activities allows us to fully understand the charge-compensation mechanism and to clearly compare the kinetics of the participating elements. The oxygen anion shows a compatible reaction rate as metal cations, whereas the Ni shows tardy oxidation at a high current density. Remarkably, the NPD and DFT calculations revealed that the formation of oxygen vacancy is the key to Li kinetics. The reduction of tetrahedral Li formation and the low *o-t-o* migration barriers caused by the existence of oxygen vacancy at low current densities explain the superior reversibility and high-rate performance compared with high current densities. Such a deep understanding is essential for adequately utilizing high-capacity cationic/anionic redox cathodes beyond the labs and enabling their commercial application.

Acknowledgement

X. H. and R. K. were supported by the Assistant Secretary for Energy Efficiency and Renewable Energy, Vehicle Technologies Office, under the Advanced Battery Materials Research (BMR) Program of the US Department of Energy under Contract No. DE-AC02-05CH11231. Computational studies by Z. Z. and A. J. were funded by the U.S. Department of Energy, Office of Science, Office of Basic Energy Sciences, Materials Sciences and Engineering Division under Contract No. DE-AC02-05-CH11231 (Materials Project program KC23MP). This research used resources of the National Energy Research Scientific Computing Center (NERSC), a U.S. Department of Energy Office of Science User Facility located at Lawrence Berkeley National Laboratory, operated under Contract No. DE-AC02-05CH11231 using NERSC award BES-ERCAP0018557. Soft X-ray spectroscopy results were collected at the Advanced Light Source, a US DOE Office of Science User Facility under contract no. DE-AC02-05CH11231. Research at Lawrence Berkeley National Laboratory is partially supported by the Energy Biosciences Institute through the EBI-Shell program.

References:

1 M. D. Radin, S. Hy, M. Sina, C. Fang, H. Liu, J. Vinckeviciute, M. Zhang, M. S. Whittingham and Y. S. Meng, *Adv. Energy Mater.*, 2017, **7**, 1602888.

2 J. Wang, X. He, E. Paillard, N. Laszczynski, J. Li and S. Passerini, *Adv. Energy Mater.*, 2016, **6**, 1600906.

3 E. Hu, X. Yu, R. Lin, X. Bi, J. Lu, S. Bak, K. W. Nam, H. L. Xin, C. Jaye, D. A. Fischer, K. Amine and X.

Q. Yang, *Nat. Energy*, 2018, **3**, 690–698.

4 P. K. Nayak, E. M. Erickson, F. Schipper, T. R. Penki, N. Munichandraiah, P. Adelhelm, H. Sclar, F. Amalraj, B. Markovsky and D. Aurbach, *Adv. Energy Mater.*, 2018, **8**, 1702397.

5 S. Hy, H. Liu, M. Zhang, D. Qian and B. Hwang, *Energy Environ. Sci.*, 2016, **9**, 1931–1954.

6 W. Zuo, M. Luo, X. Liu, J. Wu, L. Haodong, J. Li, M. Winter, R. Fu, W. Yang and Y. Yong, *Energy Environ. Sci.*, 2020, **13**, 4450–4497.

7 J. M. Tarascon, G. Vaughan, Y. Chabre, L. Seguin, M. Anne, A. P. Strobel and G. B. Amatucci, *J. Solid State Electrochem.*, 1999, **147**, 410–420.

8 L. Batteries, G. Lee, J. Wu, D. Kim, K. Cho, M. Cho, W. Yang and Y. Kang, *Angew. Chemie*, 2020, **59**, 8681–8688.

9 B. Qiu, M. Zhang, Y. Xia, Z. Liu and Y. S. Meng, *Chem. Mater.*, 2017, **29**, 908–915.

10 J. Ni, A. Dai, Y. Yuan, L. Li and J. Lu, *Matter*, 2020, **2**, 1366–1376.

11 Y. Tang, Y. Zhang, W. Li, B. Ma and X. Chen, *Chem. Soc. Rev.*, 2015, **44**, 5926–5940.

12 R. Ruess, S. Schweidler, H. Hemmelmann, G. Conforto, A. Bielefeld, D. A. Weber, J. Sann and M. T. Elm, *J. Electrochem. Soc.*, 2020, **167**, 100532.

13 G. Assat, D. Foix, C. Delacourt, A. Iadecola, R. Dedryvère and J. M. Tarascon, *Nat. Commun.*, 2017, **8**, 1–12.

14 M. Sathiya, A. M. Abakumov, D. Foix, G. Rousse, K. Ramesha, M. Saubanere, M. L. Doublet, H. Vezin, C. P. Laisa, A. S. Prakash, D. Gonbeau, G. Vantendeloo and J.-M. Tarascon, *Nat. Mater.*, 2015, **14**, 230–238.

15 Y. Zhu and C. Wang, *J. Phys. Chem. C*, 2010, **114**, 2830–2841.

16 F. Marchini, D. Rubi, M. Pozo, F. J. Williams and E. J. Calvo, *J. Phys. Chem. C*, 2016, **120**, 15875–15883.

17 K. Märker, P. J. Reeves, C. Xu, K. J. Griffith and C. P. Grey, *Chem. Mater.*, 2019, **31**, 2545–2554.

18 C. Genevois, H. Koga, L. Croguennec, M. Ménétrier, C. Delmas and F. Weill, *J. Phys. Chem. C*, 2015, **119**, 75–83.

19 J. Zheng, P. Xu, M. Gu, J. Xiao, N. D. Browning, P. Yan, C. Wang and J. Zhang, *Chem. Mater.*, 2015, **27**, 1381–1390.

20 G. Assat, C. Delacourt, D. A. D. Corte and J.-M. Tarascon, *J. Electrochem. Soc.*, 2016, **163**, A2965–A2976.

21 G. Assat and J. M. Tarascon, *Nat. Energy*, 2018, **3**, 373–386.

22 Z. W. Lebens-higgins, H. Chung, M. J. Zuba, J. Rana, Y. Li, N. V Faenza, N. Pereira, B. D. Mccloskey, F. Rodolakis, W. Yang, M. S. Whittingham, G. G. Amatucci, Y. S. Meng, T. Lee and L. F. J. Piper, *J. Phys. Chem. Lett.*, 2020, **11**, 2106–2112.

23 S. Roychoudhury, R. Qiao, Z. Zhuo, Q. Li, Y. Lyu, J. Kim, J. Liu, E. Lee and B. J. Polzin, *Energy Environ. Mater.*, 2020, **2**, 12119.

24 K. Dai, J. Wu, K. Dai, J. Wu, Z. Zhuo, Q. Li, S. Sallis, J. Mao and G. Ai, *Joule*, 2019, **3**, 518–541.

25 J. Wu, Z. Zhuo, X. Rong, K. Dai, Z. Lebens-Higgins, S. Sallis, F. Pan, L. F. J. Piper, G. Liu, Y. de Chuang, Z. Hussain, Q. Li, R. Zeng, Z. xun Shen and W. Yang, *Sci. Adv.*, 2020, **6**, 1–12.

26 G. Assat, A. Iadecola, D. Foix and J. Tarascon, *ACS Energy Lett.*, 2018, **3**, 2721–2728.

27 W. E. Gent, K. Lim, Y. Liang, Q. Li, T. Barnes, S. J. Ahn, K. H. Stone, M. McIntire, J. Hong, J. H. Song, Y. Li, A. Mehta, S. Ermon, T. Tyliszczak, D. Kilcoyne, D. Vine, J. H. Park, S. K. Doo, M. F. Toney, W. Yang, D. Prendergast and W. C. Chueh, *Nat. Commun.*, 2017, **8**, 1–12.

28 S. E. Renfrew and B. D. McCloskey, *J. Am. Chem. Soc.*, 2017, **139**, 17853–17860.

29 S. Ramakrishnan, B. Park, J. Wu, W. Yang and B. D. McCloskey, *J. Am. Chem. Soc.*, 2020, **142**, 8522–

8531.

30 X. Yu, Y. Lyu, L. Gu, H. Wu, S. M. Bak, Y. Zhou, K. Amine, S. N. Ehrlich, H. Li, K. W. Nam and X. Q. Yang, *Adv. Energy Mater.*, 2014, **4**, 1300950.

31 E. Castel, E. J. Berg, M. El Kazzi, P. Novak and C. Villevieille, *Chem. Mater.*, 2014, **26**, 5051–5057.

32 K. Luo, M. R. Roberts, R. Hao, N. Guerrini, D. M. Pickup, Y. S. Liu, K. Edström, J. Guo, A. V. Chadwick, L. C. Duda and P. G. Bruce, *Nat. Chem.*, 2016, **8**, 684–691.

33 L. A. Montoro, M. Abbate and J. M. Rosolen, *J. Electrochem. Soc.*, 2000, **147**, 1651–1657.

34 R. Qiao, Y. Wang, P. Olalde-Velasco, H. Li, Y. S. Hu and W. Yang, *J. Power Sources*, 2015, **273**, 1120–1126.

35 Q. Li, R. Qiao, L. A. Wray and J. Chen, *J. Phys. D. Appl. Phys.*, 2016, **49**, 413003.

36 W.-S. Yoon, M. Balasubramanian, K. Y. Chung, X.-Q. Yang, J. McBreen, C. P. Grey and D. A. Fischer, *J. Am. Chem. Soc.*, 2005, **127**, 17479–17487.

37 W. Yang and T. P. Devereaux, *J. Power Sources*, 2018, **389**, 188–197.

38 S. M. Butorin, J. Guo, N. Wassdahl and E. J. Nordgren, *J. Electron Spectros. Relat. Phenomena*, 2000, **111**, 235–273.

39 Z. Zhuo, C. Das Pemmaraju, J. Vinson, C. Jia, B. Moritz, I. Lee, S. Sallies, Q. Li, J. Wu, K. Dai, Y. Chuang, Z. Hussain, F. Pan, T. P. Devereaux and W. Yang, *J. Phys. Chem. Lett.*, 2018, **9**, 6378–6384.

40 Z. Zhuo, Y. Liu, J. Guo, Y. Chuang, F. Pan and W. Yang, *J. phy*, 2020, **11**, 2618–2623.

41 P. M. Csernica, S. S. Kalirai, W. E. Gent, K. Lim, Y. S. Yu, Y. Liu, S. J. Ahn, E. Kaeli, X. Xu, K. H. Stone, A. F. Marshall, R. Sinclair, D. A. Shapiro, M. F. Toney and W. C. Chueh, *Nat. Energy*, 2021, **6**, 642–652.

42 Z. Zhuo, K. Dai, R. Qiao, R. Wang, J. Wu, Y. Liu, J. Peng, L. Chen, Y. de Chuang, F. Pan, Z. xun Shen, G. Liu, H. Li, T. P. Devereaux and W. Yang, *Joule*, 2021, **5**, 975–997.

43 X. He, J. Wang, R. Kloepsch, S. Krueger, H. Jia, H. Liu, B. Vortmann and J. Li, *Nano Res.*, 2014, **7**, 110–118.

44 H. Liu, H. Liu, I. D. Seymour, N. Chernova, K. M. Wiaderek, N. M. Trease, S. Hy, Y. Chen, K. An, Z. Liu, P. J. Chupas, K. W. Chapman, M. S. Whittingham, P. Grey and Y. Shirley, *J. Mater. Chem. A*, 2018, **6**, 4189–4198.

45 H. Liu, C. R. Fell, K. An, L. Cai and Y. Shirley, *J. Power Sources*, 2013, **240**, 772–778.

46 H. Liu, Y. Chen, S. Hy, K. An, S. Venkatachalam, D. Qian, M. Zhang and Y. S. Meng, *Adv. Energy Mater.*, 2016, **6**, 1502143.

47 F. Dogan, B. R. Long, J. R. Croy, K. G. Gallagher, H. Iddir, J. T. Russell, M. Balasubramanian and B. Key, *J. Am. Chem. Soc.*, 2015, **137**, 2328–2335.

48 B. Xu, C. R. Fell, M. Chi and Y. S. Meng, *Energy Environ. Sci.*, 2011, **4**, 2223–2233.

49 C. Chen, W. Ye, Y. Zuo, C. Zheng and S. P. Ong, *Chem. Mater.*, 2019, **31**, 3564–3572.

50 D. Qian, B. Xu, M. Chi and Y. S. Meng, *Phys. Chem. Chem. Phys.*, 2014, **16**, 14665–14668.

51 H. Yu, Y. Wang, D. Asakura, E. Hosono, T. Zhang and H. Zhou, *RSC Adv.*, 2012, **2**, 8797–8807.

52 K. Kang, Y. S. Meng, J. Breger, C. P. Grey and G. Ceder, *Science (80-.).*, 2006, **311**, 977–981.

53 R. Nölle, K. Beltrop, F. Holtstiege, J. Kasnatscheew, T. Placke and M. Winter, *Mater. Today*, 2020, **32**, 131–146.

54 H. Liu, H. Liu, I. D. Seymour, N. Chernova, K. M. Wiaderek, N. M. Trease, S. Hy, Y. Chen, K. An, Z. Liu, P. J. Chupas, K. W. Chapman, M. S. Whittingham, P. Grey and Y. Shirley, *J. Mater. Chem. A*, 2018, **6**, 4189–4198.

55 R. Qiao, Q. Li, Z. Zhuo, S. Sallis, O. Fuchs, M. Blum, L. Weinhardt, J. Pepper, M. Jones, A. Brown, A. Spucces, K. Chow, F. Pan, L. F. J. Piper, P. Glans, Y. Chen, S. Yan, M. Blum, L. Weinhardt, C. Heske, J. Pepper, M. Jones, A. Brown, A. Spucces, K. Chow, B. Smith, P. Glans, Y. Chen, S. Yan, F. Pan, L. F. J. Piper and J. Denlinger, *Rev. Sci. Instrum.*, 2017, **88**, 033106.

56 K. E. An, H. D. Skorpenske, A. D. Stoica, D. Ma, X. Wang and E. Cakmak, *Metall. Mater. Trans. A*, 2011, **42A**, 95–99.

57 B. H. Toby, *J. Appl. Crystallogr.*, 2001, **34**, 210–213.

58 A. C. Larson and R. B. V. Dreele, *Los Alamos Natl. Lab. Rep.*, 2004, 86–748.

59 W. Kohn and L. J. Sham, *Phys. Rev.*, 1965, **140**, A1133–A1138.

60 G. Kresse and J. Furthmueller, *Phys. Rev. B*, 1995, **54**, 11169–11186.

61 P. E. Blöchl, *Phys. Rev. B*, 1994, **50**, 17953–17979.

62 J. P. Perdew, K. Burke and M. Ernzerhof, *Phys. Rev. Lett.*, 1996, **77**, 3865–3868.

63 A. K. Padhi, K. S. Nanjundaswamy and J. B. Goodenough, *J. Electrochem. Soc.*, 1997, **144**, 1188–1194.

64 a. I. Lichtenstein, V. I. Anisimov and J. Zaanen, *Phys. Rev. B*, 1995, **52**, 5467–5471.

65 A. Jain, S. P. Ong, G. Hautier, W. Chen, W. D. Richards, S. Dacek, S. Cholia, D. Gunter, D. Skinner, G. Ceder and K. A. Persson, *APL Mater.*, 2013, **1**, 1–11.

66 G. L. W. Hart and R. W. Forcade, *Phys. Rev. B - Condens. Matter Mater. Phys.*, 2008, **77**, 1–12.

67 S. P. Ong, W. D. Richards, A. Jain, G. Hautier, M. Kocher, S. Cholia, D. Gunter, V. L. Chevrier, K. A. Persson and G. Ceder, *Comput. Mater. Sci.*, 2013, **68**, 314–319.

68 L. Yang, C. Chen, S. Xiong, C. Zheng, P. Liu, Y. Ma, W. Xu, Y. Tang, S. P. Ong and H. Chen, *JACS Au*, 2021, **1**, 98–107.

69 G. Henkelman and H. Jónsson, *J. Chem. Phys.*, 2000, **113**, 9978–9985.

Supporting Information

Chemical and structural evolutions of Li-Mn-rich layered electrodes under different current densities

Xin He[a,b,c#], Jue Wu[d,e#], Zhuoying Zhu[b#], Haodong Liu[f], Ning Li[b], Dong Zhou[g], Xu Hou[h], Jun Wang[g], Haowei Zhang[c], Dominic Bresser[i], Yanbao Fu[b], Matthew J Crafton[b,j], Bryan D McCloskey[b,j], Yan Chen[k], Ke An[k], Ping Liu[f], Anubhav Jain[b*], Jie Li[l*], Wanli Yang[d*], Yong Yang[e], Martin Winter[g,h], Robert Kostecki[b*]

a. School of Chemical Engineering at Sichuan University, Chengdu, 610065, China
b. Energy Storage & Distributed Resources Division, Lawrence Berkeley National Laboratory, 1 Cyclotron Road, Berkeley, CA, 94720, USA
c. College of Electrical Engineering at Sichuan University, Chengdu, 610065, China
d. Advanced Light Source, Lawrence Berkeley National Laboratory, Berkeley, California 94720, United States
e. State Key Laboratory for Physical Chemistry of Solid Surfaces, Department of Chemistry, College of Chemistry and Chemical Engineering, Xiamen University, Xiamen 361005, China
f. Department of Nanoengineering, University of California San Diego, La Jolla, CA, 92093, United States
g. MEET Battery Research Center, Institute of Physical Chemistry, University of Münster, Corrensstraße 46, 48149 Münster, Germany
h. Helmholtz Institute Münster – Forschungszentrum Jülich GmbH (IEK 12), Corrensstrasse 46, 48149 Münster, D-48149 Münster, Germany
i. Helmholtz Institute Ulm (HIU), Ulm 89081, Germany
j. Department of Chemical and Biomolecular Engineering, College of Chemistry, University of California, Berkeley, CA, 94720, United States
k. Neutron Scattering Division, Oak Ridge National Laboratory, Oak Ridge, TN, 37830, USA
l. Department of Energy, Politecnico di Milano, Via Lambruschini 4, Milano, 20156, Italy

[#] These authors made equal contributions
* Corresponding author

Experimental

Material synthesis.

The Li-Mn-rich layered oxide $Li_{1.2}Ni_{0.16}Co_{0.08}Mn_{0.56}O_2$ was prepared by a co-precipitation method followed by a high-temperature annealing procedure. $NiSO_4 \cdot 6H_2O$, $CoSO_4 \cdot 7H_2O$, and $MnSO_4 \cdot 4H_2O$ (2:1:7 in molar) were dissolved in distilled water to form a solution. Then, a mix of Li_2CO_3 and NH_4OH solution was pumped into a continuously stirring tank reactor (CSTR) at room temperature. The resulting precipitates were washed several times with distilled water to remove residual Li^+. After being dried in a vacuum oven at 80 ^oC for over 12 h, Stoichiometric amounts of the $(Ni_{0.2}Co_{0.1}Mn_{0.7})CO_3$ precipitate and Li_2CO_3 were thoroughly mixed at a molar ratio of 1:0.55 to form the precursor powders. The precursor was first heated at 500 ^oC for 5h, then calcined at

850 ^{o}C in the air for 15h, and finally cooled to room temperature, naturally.

Electrochemical measurements.

Electrodes were prepared by casting a slurry with the composition of 80 wt% $Li_{1.2}Ni_{0.16}Co_{0.08}Mn_{0.56}O_2$ active material, 10 wt% Super C65 and 10 wt% PVdF on aluminum foil. After drying under vacuum at 110 ^{o}C overnight, the electrode sheet has been punched to ∅ 12 mm discs. The average mass loading of active material was about 2.5 mg cm^{-2}. The electrodes were assembled into two-electrodes T-cells[53] with pre-activated lithium foil as a counter electrode. 100µl 1M $LiPF_6$ in 1:1(wt %) ethylene carbonate (EC): dimethyl carbonate (DMC) was added as electrolyte. The lithium foil was first electro-deposited in a symmetric cell at 0.5 mA cm^{-2} for 2 hours to lower the influence of solid electrolyte interphase (SEI)[54] formation on the lithium electrode. The cells were disassembled after electrochemical test, and electrodes were washed twice by DMC solvent. Then the electrodes were dried at 60°C under vacuum and kept at Ar atmosphere for further measurements.

Synchrotron sXAS and mRIXS measurements.

Soft XAS measurements were carried out on beamline 10-1 at SSRL. Ni, Co, and Mn L-edge spectra were acquired under an ultrahigh vacuum (10^{-9} Torr) in a single load at room temperature using total electron yield (TEY) via the drain current and fluorescence yield (TFY) via Silicon Photodiodes. All the TEY and TFY spectra were normalized to the beam flux measured by the gold mesh. The resolution of the excitation energy was 0.15 eV.

The O *K*-edge sXAS and mRIXS data were collected in the iRIXS endstation at Beamline 8.0.1 of Advanced Light Source (ALS) at Lawrence Berkeley National Laboratory (LBNL).[55] For mRIXS experiments, to avoid air exposure, the cycled cathodes were disassembled and mounted in an Ar-filled glove box. The samples were transferred to the experimental vacuum chamber via a homemade sample transfer kit to avoid any air exposure. All data were collected from the side of the electrodes facing the current collector by cleaving the electrode. The lowest possible incident beam flux was used with samples keep moving to eliminate the possible irradiation effect and to collect the signals over a large area of electrodes. The mRIXS maps were obtained after energy calibration and normalization to collection time and incident X-ray beam flux, through a multi-step data process.

mRIXS -sPFY data. The O *K*-edge mRIXS-sPFY profiles were obtained via integrating the mRIXS intensity in the range of emission energy from 523 to 524 eV, where the oxidized-oxygen feature appeared. In order to quantify the oxidized-oxygen feature, the area of the mRIXS-sPFY feature was measured (Table S1) by integrating the peak area from 530 to 532 eV excitation energy, with a peak intensity normalization at 529.8 eV excitation energy. Details and demonstrations of this analysis have been reported previously[24]**.**

Neutron diffraction. Time of flight (TOF) powder neutron diffraction data was collected at the VULCAN instrument at the Spallation Neutron Source (SNS), Oak Ridge National Laboratory.[56] At VULCAN, approximately 1.6g of the powder sample was loaded into a vanadium sample can of 6mm diameter in a helium-filled glove box. An incident beam (5 mm × 12 mm) of 0.7 to 3.5 Å bandwidth, allowing 0.5~2.5

Å d-space in the diffracted pattern of the ±90◦ 2θ detector banks, was selected using the double-disk choppers at 30 Hz frequency. The high-resolution mode was employed with delta d/d ~0.25%. The SNS was at nominal, 1400 kW, power. Powder neutron diffraction data were collected in the high-resolution mode for a duration of 3 h and processed using VDRIVE software. The data were normalized to a vanadium rod. Rietveld refinement of the neutron diffraction data was performed using GSAS software with EXPGUI interface.[57,58]

Operando DEMS.

The Operando DEMS experiment was carried out in a sealed electrochemical cell. The positive electrodes were prepared with mass of around 8 mg. The assembled cell was electrochemical controlled by Land CT 2001A battery testers in room temperature. During the measurement, high-purity argon gas flowed through the main chamber of the cell as the carrier gas and were detected using the quadrupole mass spectrometer (Hiden Analytical), the flow rate was controlled at 0.6 mL min-1 using a digital mass flow meter. The detected CO2 and O2 were quantified via the known amounts of reference gases.

Calculation details.

All DFT[59] calculations were performed using the Vienna ab initio simulation package (VASP)[60]with the projector augmented wave (PAW) method[61]. The Perdew–Burke–Ernzerhof (PBE) generalized gradient approximation (GGA) functional[62] with a Hubbard *U* extension of 3.9 eV for manganese, 3.32 eV for cobalt and 6.2 eV for nickel was adopted for structural relaxations and energy calculations[63,64]. All calculations were initialized in a ferromagnetic high-spin configuration because the energy affected by antiferromagnetic ordering is very small (< 3 meV/atom) based on our calculations. A plane wave energy cutoff of 520 eV and k-point density of at least 1,000/*n*, where *n* is the number of atoms in the unit cell, was used for initial relaxations. These settings are consistent with those used for the Materials Project[65]. The energies and forces were converged to 10^{-5} eV per cell and 0.05 eV $Å^{-1}$, respectively.

Structure enumeration and relaxation

To prepare the pristine structure of $Li_{1.2}Ni_{0.16}Co_{0.08}Mn_{0.56}O_2$, a 3 × 2 × 2 supercell of the $Li_{1+\alpha}M_{1-\alpha}O_2$ (M=Ni, Mn, Co) primitive cell (space group: R-3m) was created, which is 12 formula units of $Li_{1+\alpha}M_{1-\alpha}O_2$. In the transition metal layer, the occupancy of cations was set as Li: Ni: Co: Mn = 2:2:1:7, whereas the Li layer was fully occupied by 12 Li atoms (with supercell formula $Li_{14}Ni_2CoMn_7O_{24}$). All symmetrically distinct *TM* layer orderings were generated by the enumlib[66] package in Python Materials Genomics (pymatgen)[67]. Due to the large number of cation orderings (>1000), we applied the MatErials Graph Network (MEGNET[49]) deep learning model to screen out low-energy configurations.[68] A group of 100 random structures with distinct cation arrangements were used for the DFT-energy vs. MEGNET-energy parity plot after structural relaxations (Figure S11). Then the low-energy configurations (E_{hull} < 5 meV/atom) were relaxed with the PBE+*U* functional to obtain the ground-state pristine Li-rich NCM structure for the following calculations.

The initial charge-discharge cycle with different rates (10C vs. 0.1C) leads to two delithiated phases based on the amount of O_2 (0% vs. 4%) released from the pristine Li-rich NCM. The Li content was fixed to x~0.83 for DFT calculations, where O_2 started to be released at 4.42V-4.8V plateau region under 0.1C[46]. To obtain this composition of $Li_{10}Ni_2CoMn_7O_{24}$ ($Li_{8/12}[Li_{2/12}Ni_{2/12}Co_{1/12}Mn_{7/12}]O_2$), we extracted 4/12 Li ions in the Li layer from the ground-state $Li_{14}Ni_2CoMn_7O_{24}$ ($Li[Li_{2/12}Ni_{2/12}Co_{1/12}Mn_{7/12}]O_2$) structure (see **Figure 5**). The other Li ions in the TM layers remain in their positions which matches with the experimental refinement results in Table S5, S6. Different Li orderings in $Li_{10}Ni_2CoMn_7O_{24}$ ($Li_{8/12}[Li_{2/12}Ni_{2/12}Co_{1/12}Mn_{7/12}]O_2$) were fully relaxed and the lowest-energy configuration was used for the following oxygen vacancy generation and NEB calculations.

To mimic 4% oxygen vacancy in $Li_{0.83}Ni_{0.16}Co_{0.08}Mn_{0.56}O_{1.92}$ after 0.1C charge-discharge cycle, we sequentially extracted 2/48 oxygen atoms in a 3 × 4 × 2 supercell, leading to the formula of $Li_{20}Ni_4Mn_{14}Co_2O_{46}$ ($Li_{8/12}[Li_{2/12}Ni_{2/12}Co_{1/12}Mn_{7/12}]O_{23/12}$). After removing the first oxygen atom, we found the energy is highly dependent on the local environments of oxygen vacancy, to be more specific, the nearest coordinated *TM* metals in the *TM* layer (see **Figure 6**). The electrostatic repulsion between oxygen vacancy and *TM* are increasing by order of Ni < Co < Mn.

NEB calculations

Climbing-image nudged elastic band (CI-NEB)[69]calculations were performed using 3 × 4 × 2 supercells of the LiMO_2 primitive cell. The supercell choice was applied to maximize the distance between periodic images of the paths and to match with 4% oxygen vacancy concentration as observed in the experiments. For all the NEB calculations, five linearly interpolated intermediate images of the initial guess were adopted with the energies and forces convergences of 10^{-5} eV per supercell and 0.02 eV $Å^{-1}$, respectively.

For 10C rate without oxygen vacancy, the supercell has a formula of $Li_{20}Ni_4Co_2Mn_{14}O_{48}$ (unit cell formula: $Li_{8/12}[Li_{2/12}Ni_{2/12}Co_{1/12}Mn_{7/12}]O_2$), which is roughly equivalent to $Li_{0.83}Ni_{0.16}Co_{0.08}Mn_{0.56}O_2$. We used the lowest-energy configuration from cation orderings and performed the Li vacancy *o-t-o* hops categorized by the intermediate tetrahedral site because only the local atomic arrangements, especially the face-sharing *TM*, have a substantial effect on the migration barriers[52]. The barriers for 3 symmetrically distinct paths were computed (see Figure S12 (a-c)) when the face-sharing TM is Ni, Co and Mn.

For 0.1C with 4% oxygen vacancy, the supercells we used have a formula of $Li_{20}Ni_4Co_2Mn_{14}O_{46}$ (unit cell formula: $Li_{8/12}[Li_{2/12}Ni_{2/12}Co_{1/12}Mn_{7/12}]O_{23/12}$), which is roughly equivalent to $Li_{0.83}Ni_{0.16}Co_{0.08}Mn_{0.56}O_{1.92}$. Two configurations with divacancy distances of 5.8Å (the ground-state configuration) and 3.1Å (9 meV/atom higher in energy than the ground state) were chosen to perform the *o-t-o* hops. 5 distinct paths were computed as shown in Figure S12 (d-f). The migration barriers are affected by many factors like *TM* species, the local environments of the oxygen vacancy (primary or secondary for the paths), and divacancy distances. The strong repulsion between divacancies makes it unlikely to have two vacancies within the same TMO_6 octahedron. The minimum divacancy distance we found with a reasonably low configuration energy is

~3.1Å. And this intensive local oxygen vacancy does help to reduce the migration barriers furthermore (see Figure S12 (d)).

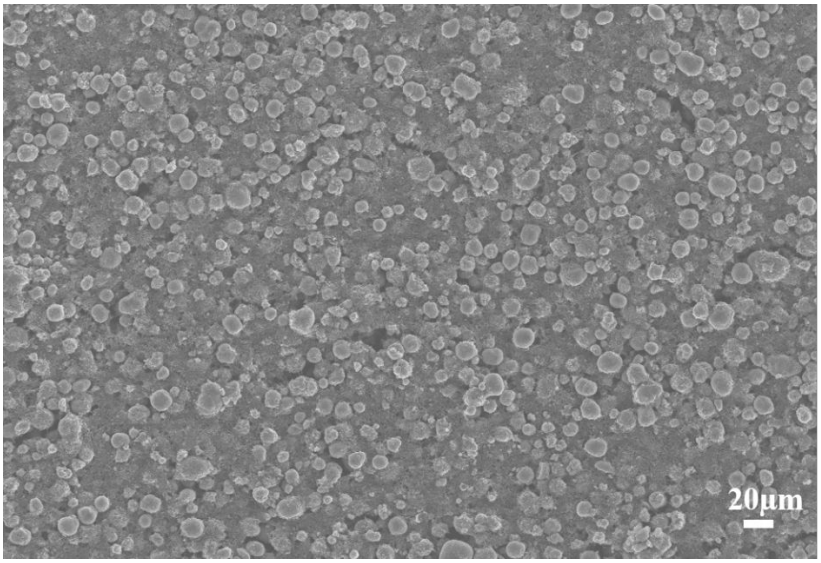

Figure S1. SEM image of the prepared electrode with LMR-NCM material

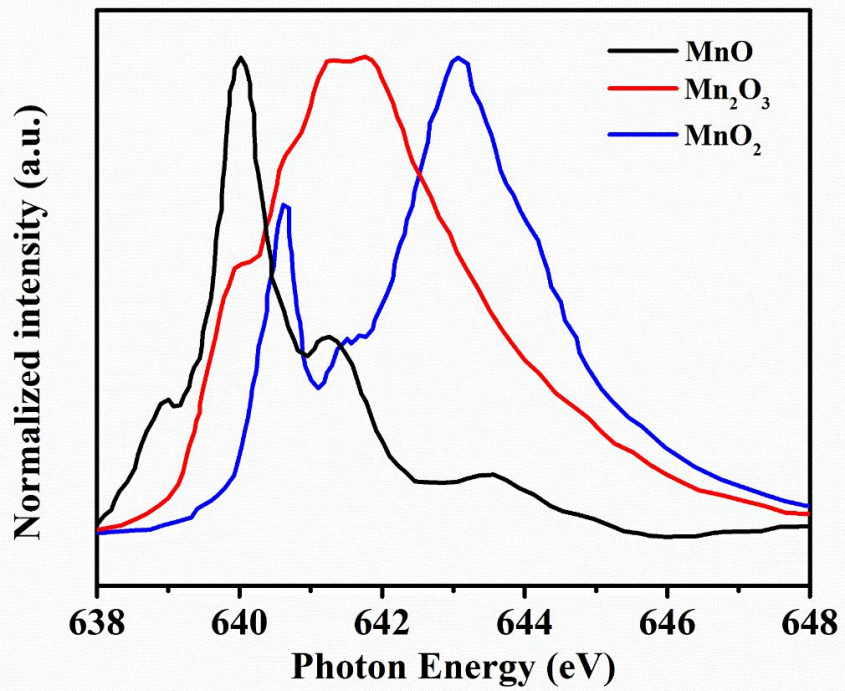

Figure S2. Mn *L*-edge sXAS spectra for MnO, Mn_2O_3, and MnO_2 as reference spectra for Mn^{2+}, Mn^{3+}, and Mn^{4+} ions, respectively.

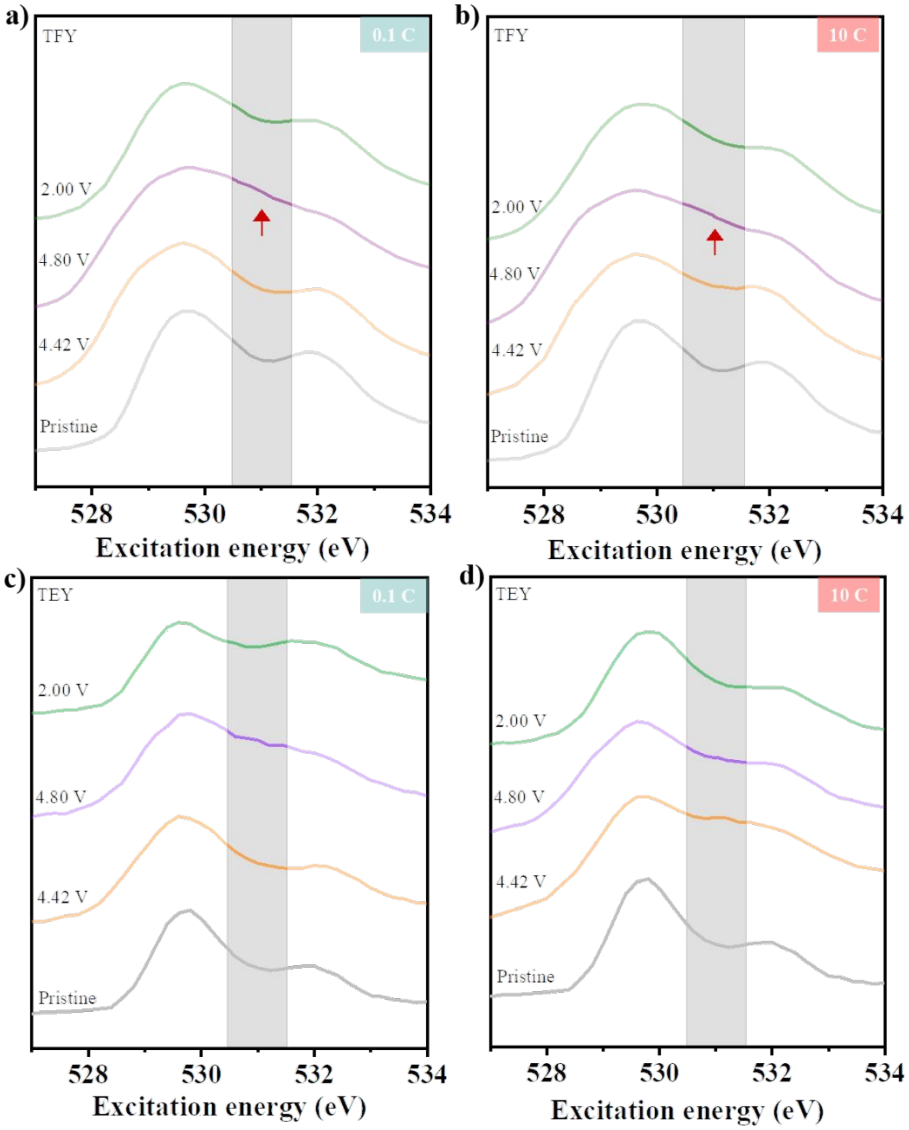

Figure S3. O K-edge sXAS spectra for Li-rich electrodes at different SOCs in TFY and TEY modes.

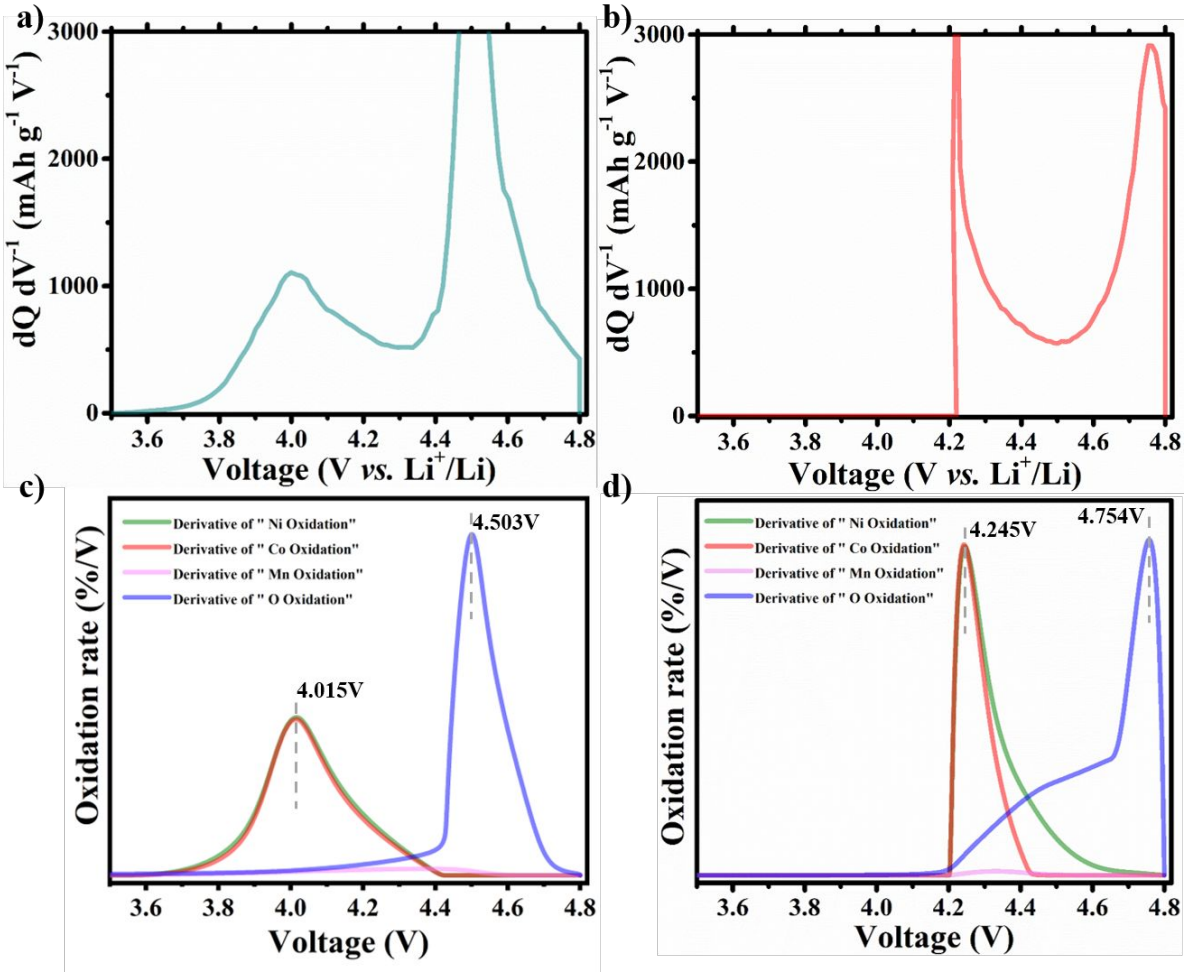

Figure S4. dQ/dV vs. voltage plots of the first charge processes at 0.1C (a) and 10C (b), and the simulation of corresponding active Li-rich materials charge compensation mechanism based on the mean valence state of involved elements.

Table S1. Peak area evolutions and corresponding delivered capacities at 0.1C and 10C

Cycle	Rate	Sample	sPFY area (a.u.)	Area change (a.u.)	Reversibility of area change	Capacity (mAh/g)	Coulombic efficiency (%)
1st		**Pristine**	0.01367	0.0000	--	--	--
	0.1C	**0.1C-4.42 V**	0.01465	0.00098	Discharge/charge: (0.01028-0.00129)/0.01028 =87.5%	102.8	92.8%
		0.1C-4.80 V	0.02395	0.01028		300.2	
		0.1C-2.00 V	0.01496	0.00129		278.4	
	10C	**10C-4.42 V**	0.01571	0.00204	Discharge/charge: (0.00945-0.00315)/0.00945 =66.7%	50.6	65.6%
		10C-4.6 V	0.01658	0.00291			
		10C-4.80 V	0.02312	0.00945		156.6	
		10C-2.00 V	0.01682	0.00315		102.7	

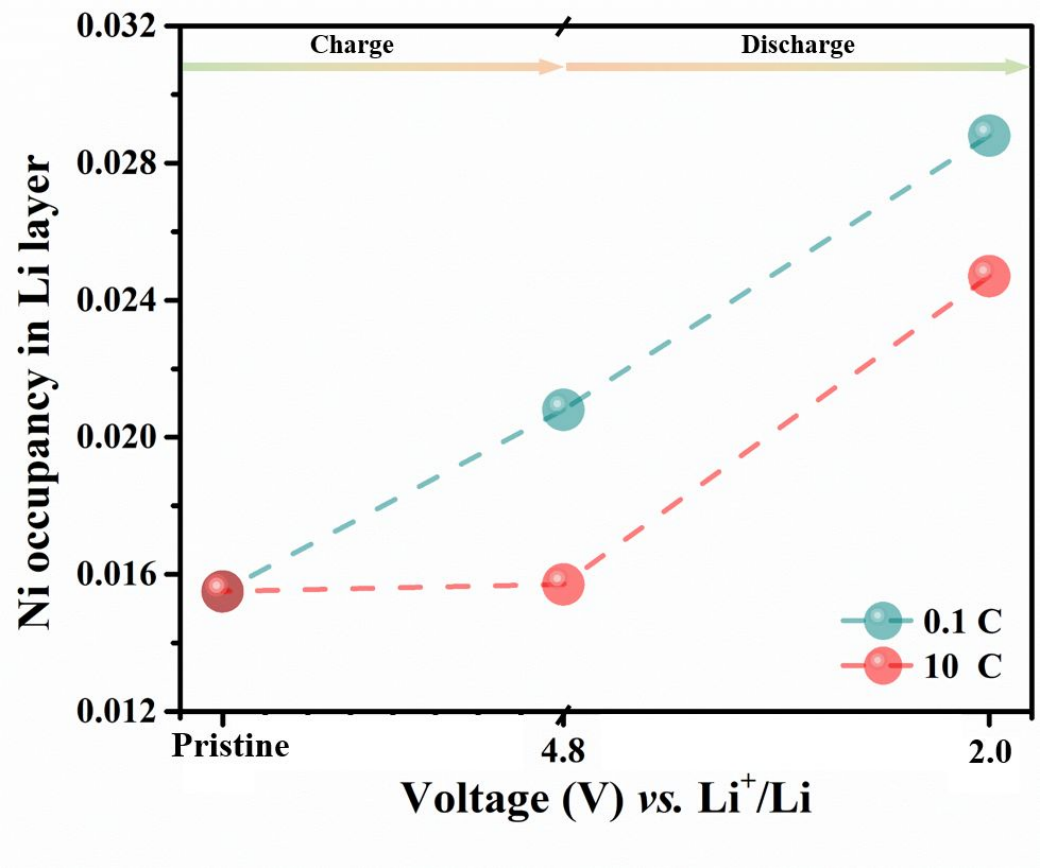

Figure S5. Refinement results of Ni occupancy in Li layer at different states with the current rates of 0.1C and 10C, respectively.

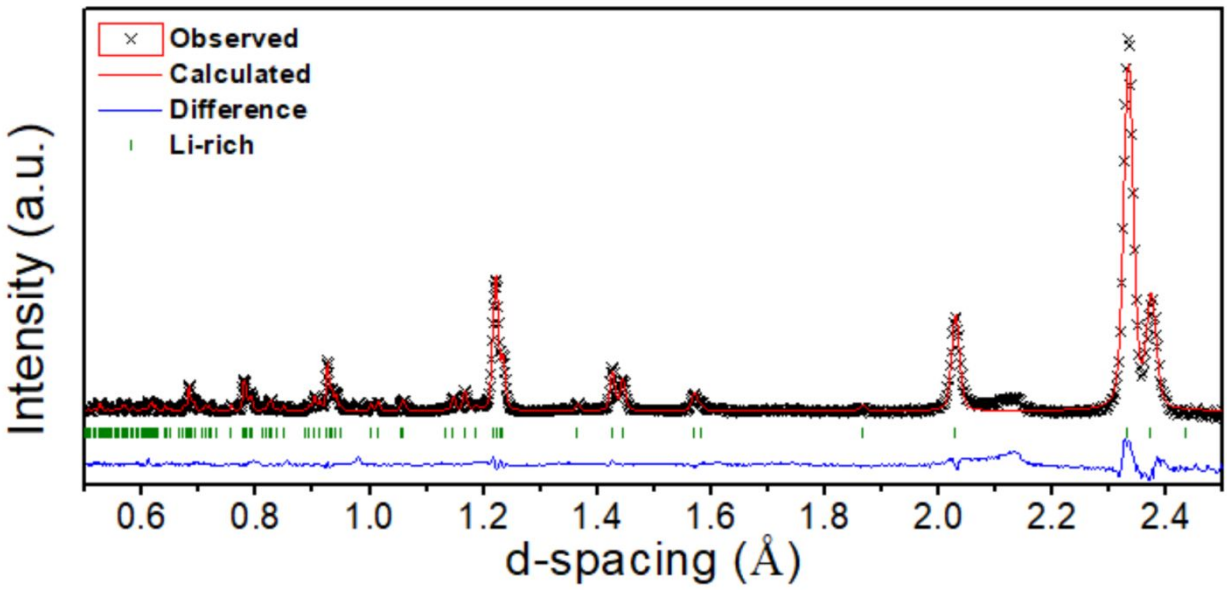

Figure S6. Refined neutron powder diffraction pattern of Li-rich material at the open circuit potential state.

Table S2. Refinement results of the Li-rich material at the open circuit voltage (OCV) state.

Space group: R-3m, R_{wp} = 4.52% **a = b = 2.8501(2) Å, c = 14.232(1) Å, α=β=90°, γ=120°**				
Atoms	Wyckoff positions			Occupancy
Li	0	0	0.5	0.215(5)
Ni	0	0	0.5	0.145(5)
Mn	0	0	0.5	0.56
Co	0	0	0.5	0.08
O	0	0	0.2412(1)	1
Li	0	0	0	0.985(5)
Ni	0	0	0	0.015(5)

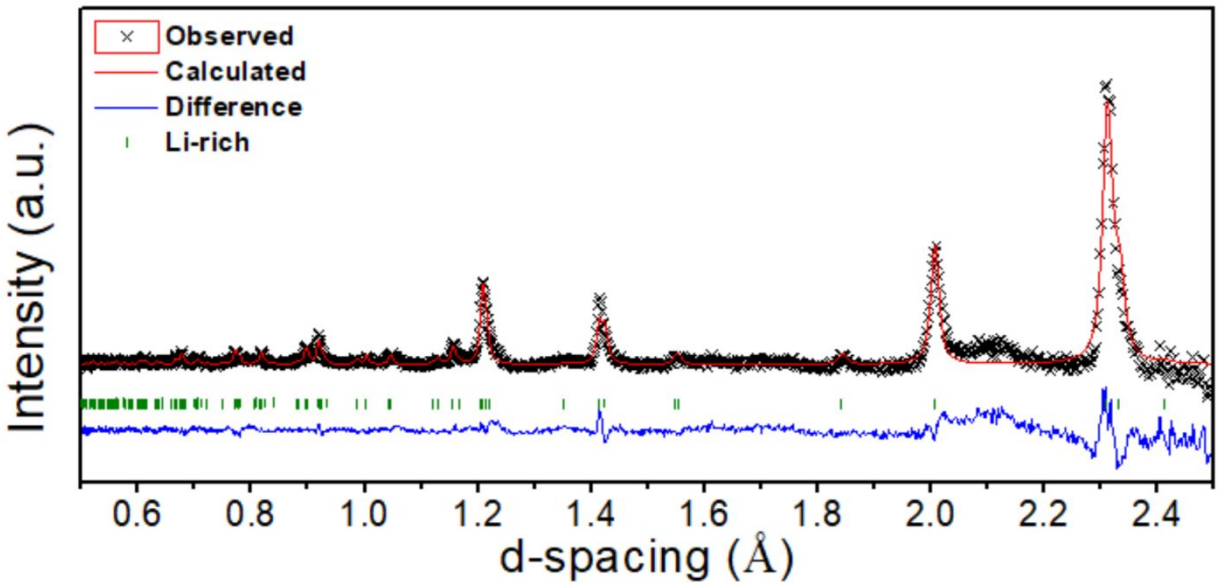

Figure S7. Refined neutron powder diffraction pattern of fully charged Li-rich material (4.8V) at 0.1C

Table S3. Refinement results of the of fully charged Li-rich material (4.8V) at 0.1C

Space group: R-3m, R_{wp} = 2.70% **a = b = 2.8259(6) Å, c = 13.990(4) Å, α=β=90°, γ=120°**				
Atoms	Wyckoff positions			Occupancy
Li	0	0	0.5	0.069(8)
Ni	0	0	0.5	0.140(8)
Mn	0	0	0.5	0.56
Co	0	0	0.5	0.08
O	0	0	0.2373(2)	0.961(9)
Li	0	0	0	0.178(8)
Ni	0	0	0	0.020(8)

.

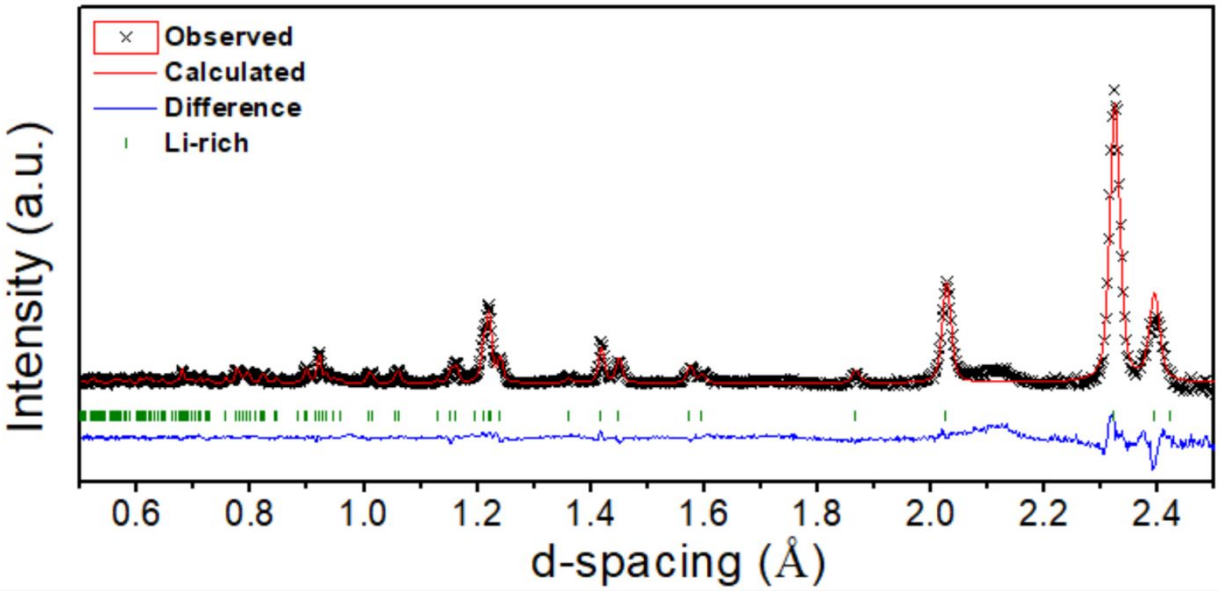

Figure S8. Refined neutron powder diffraction pattern of fully charged Li-rich material (4.8V) at 10C

Table S4. Refinement results of the of fully charged Li-rich material (4.8V) at 10C

Space group: R-3m, R_{wp} = 3.09% **a = b = 2.8345(3) Å, c = 14.354(2) Å, α=β=90°, γ=120°**				
Atoms	Wyckoff positions			Occupancy
Li	0	0	0.5	0.141(3)
Ni	0	0	0.5	0.146(3)
Mn	0	0	0.5	0.56
Co	0	0	0.5	0.08
O	0	0	0.2386(1)	0.996(9)
Li	0	0	0	0.520(3)
Ni	0	0	0	0.015(7)

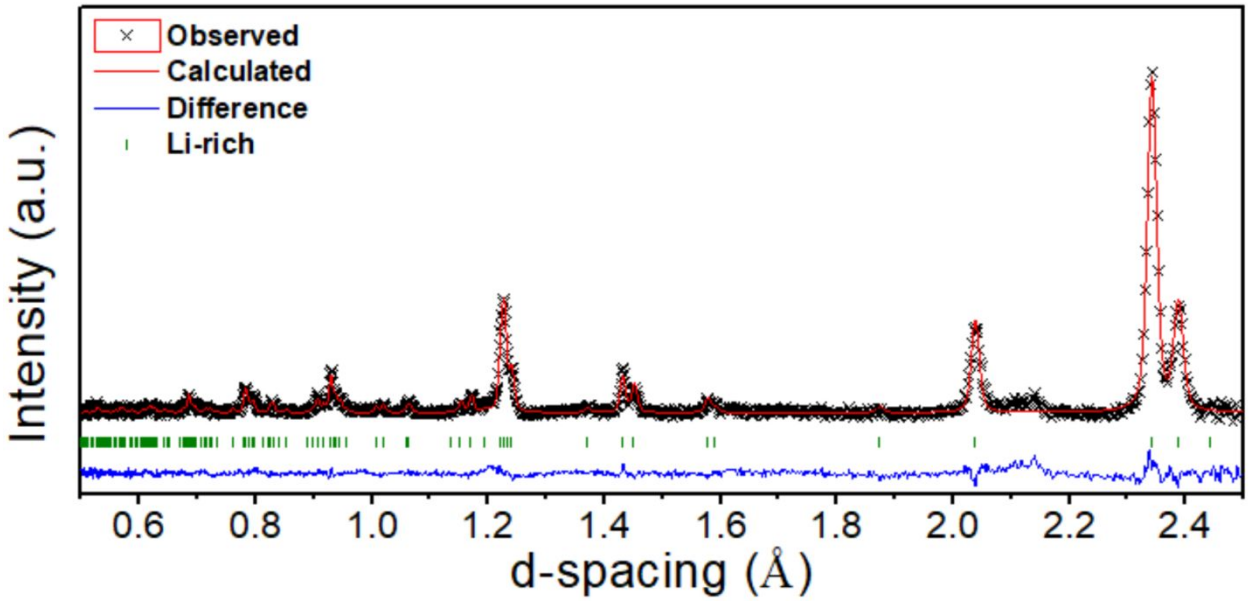

Figure S9. Refined neutron powder diffraction pattern of fully discharged Li-rich material (2V) at 0.1C

Table S5. Refinement results of the of fully discharged Li-rich material (2V) at 0.1C

Space group: R-3m, R_{wp} = 2.48% **a = b = 2.8599(3) Å, c = 14.316(2) Å, α=β=90°, γ=120°**				
Atoms	Wyckoff positions			Occupancy
Li	0	0	0.5	0.181(8)
Ni	0	0	0.5	0.132(8)
Mn	0	0	0.5	0.56
Co	0	0	0.5	0.08
O	0	0	0.2411(1)	0.961(9)
Li	0	0	0	0.949(8)
Ni	0	0	0	0.028(8)

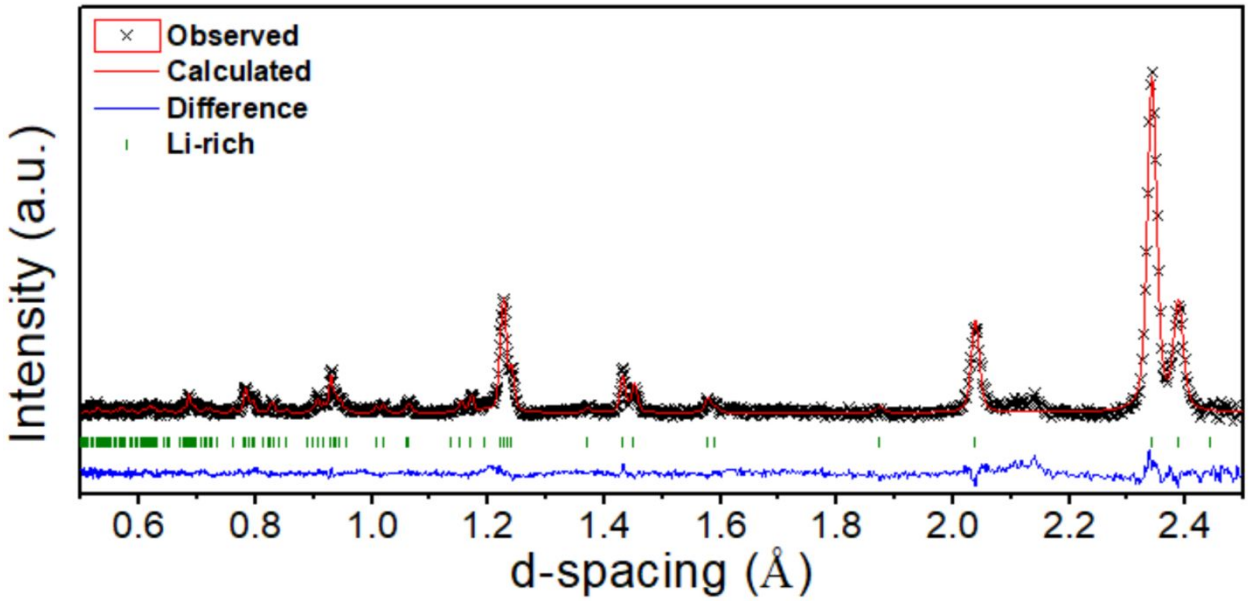

Figure S10. Refined neutron powder diffraction pattern of fully discharged Li-rich material (2V) at 10C

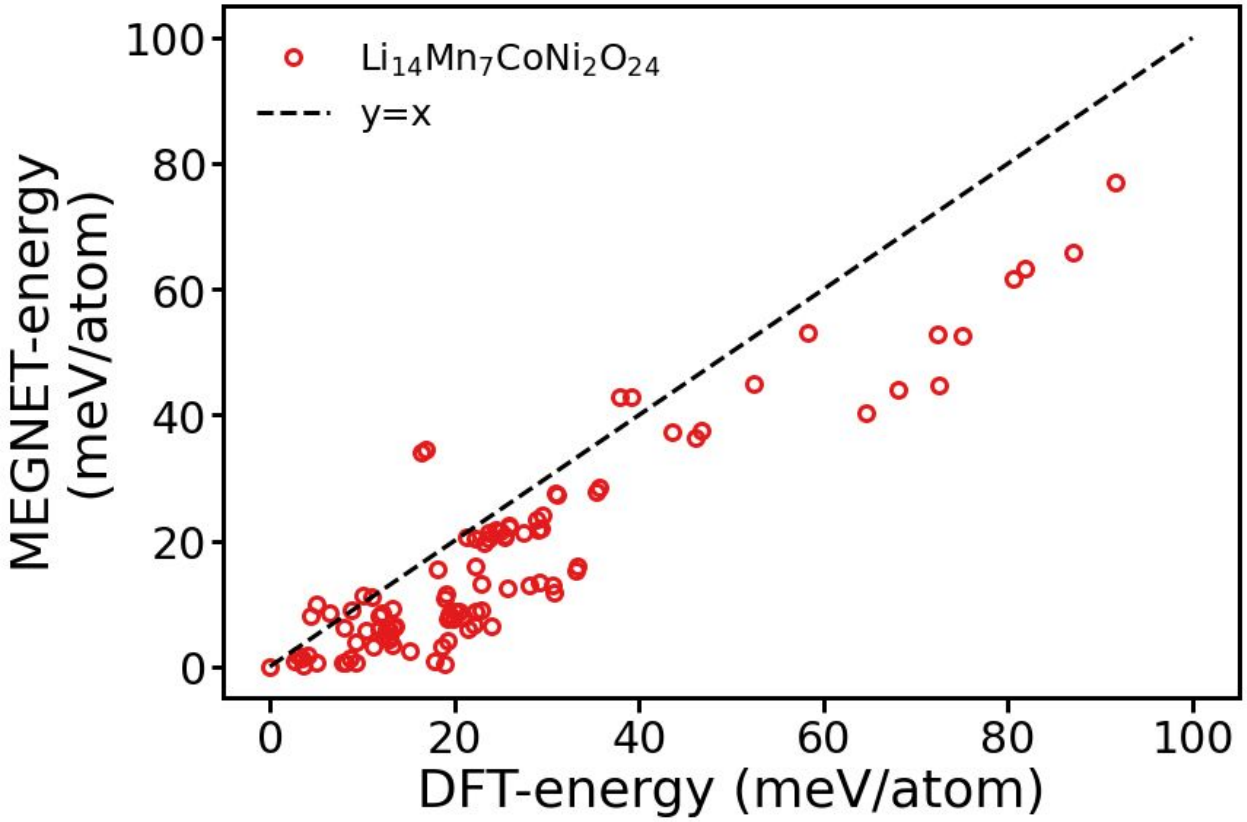

Figure S11. Parity plot of DFT-energy and MEGNET predicted energy of 100 randomly selected structures of $Li_{14}Ni_2CoMn_7O_{24}$ with different cation orderings.

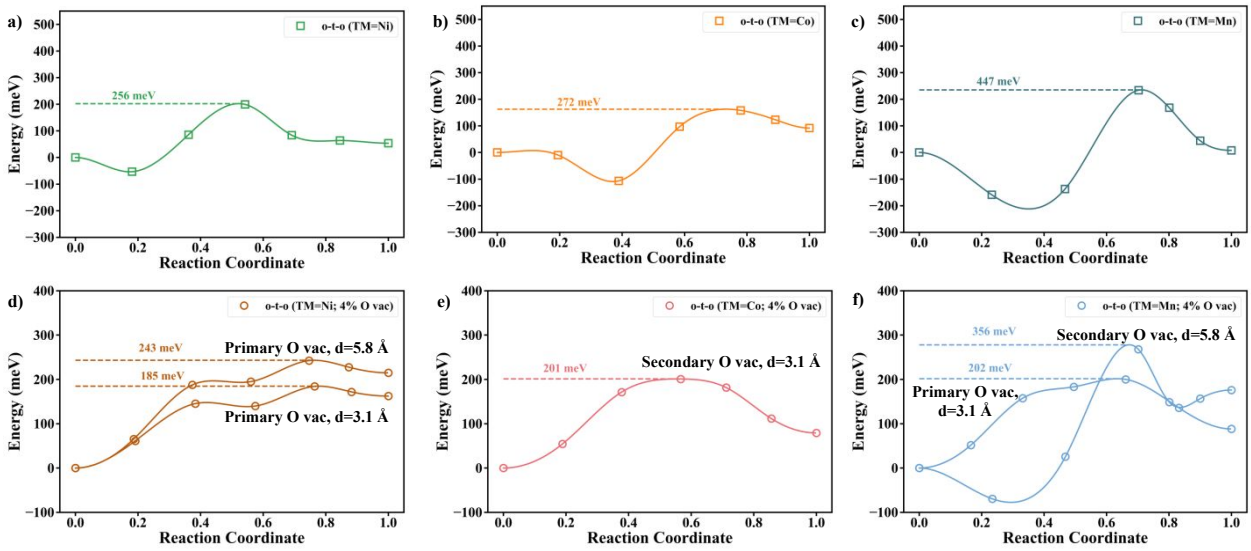

Figure S12. NEB barriers of $Li_{0.83}Ni_{0.16}Mn_{0.56}Co_{0.08}O_2$ at 10C (**a-c**) and $Li_{0.83}Ni_{0.16}Mn_{0.56}Co_{0.08}O_{1.92}$ at 0.1C (**d-f**). Panels (**a-c**) refer to the *o-t-o* migration barriers when tet site is face-sharing with a TM (TM=Ni, Co, Mn) without oxygen vacancy in the lattice. At 10C, the *o-t-o* migration barriers are ranging from 256 meV (TM=Ni) to 447 meV (TM=Mn). Panels (**d-f**) refer to the *o-t-o* migration barriers with 4% oxygen vacancy at 0.1C. The values are greatly decreased from 10C, showing the migration barriers as low as 185 meV (TM=Ni), 201 meV (TM=Co) and 202 meV (TM=Mn). Two configurations with different divacancy distances (d=3.1Å or d=5.8Å) are applied for the NEB calculations. The primary O vacancy indicates the position of oxygen vacancy (either in the oct vertex of LiO_6 or the tet vertex of intermediate LiO_4 in the *o-t-o* path as shown in Figure 7). The secondary O vacancy represents the other possible positions.

Table S6. Refinement results of the of fully discharged Li-rich material (2V) at 10C

Space group: R-3m, R_{wp} = 2.37% **a = b = 2.8490(3) Å, c = 14.311(2) Å, α=β=90°, γ=120°**				
Atoms	Wyckoff positions			Occupancy
Li	0	0	0.5	0.170(7)
Ni	0	0	0.5	0.136(7)
Mn	0	0	0.5	0.56
Co	0	0	0.5	0.08
O	0	0	0.2399(1)	0.996(9)
Li	0	0	0	0.852(7)
Ni	0	0	0	0.024(7)

Table S7 tRatio of Li vacancy in Li layer and Li vacancy in transition metal layer

0.1C			10C			
4.42V	4.8V	2.0V	4.42V	4.65V	4.8V	2.0V
25:0	62:10	3:3	13:2	21:4	35:7	10:4